Doctoral Dissertation (Censored)
博士論文 (要約)

Growth and magnetic properties of iron nitride monolayers on Cu substrates

(Cu 基板上の窒化鉄原子層の成長と磁性)

A Dissertation Submitted for the Degree of Doctor of Philosophy
December 2019

令和元年 12 月博士 (理学) 申請

Department of Physics, Graduate School of Science,
The University of Tokyo
東京大学大学院理学系研究科物理学専攻

Takuma Hattori
服部　卓磨

Abstract

With the recent discovery in the ferromagnetic two-dimensional van der Waals crystals, fabrication for the magnetic monolayers and tuning their magnetic properties by the substrates have attracted extensive attention. In order to elucidate the origin of the magnetic properties tuned by the substrates, it is necessary to grow the ferromagnetic monolayers without intermixing.

Here, we focused on the iron nitride monolayers. Due to the strong in-plane robust bonding between Fe and N atoms, the well-ordered iron nitride monolayer grows on the Cu(001) substrate without intermixing and it exhibits ferromagnetism. In the present study, we have investigated growth condition and structure of the new iron nitride monolayers and we have discussed their magnetic properties tuned by the substrates. We have combined the atomic scale observation for the surface morphology and electronic properties by scanning tunnel microscopy/spectroscopy (STM/STS) with the element specific study on the magnetic properties by X-ray absorption spectra and X-ray magnetic circular dichroism (XAS/XMCD).

First, we have investigated the growth and structure of the iron nitride film on the Cu(111) substrate by using STM. At the high annealing temperature, we observed the square Fe_2N monolayer on the Cu(111) substrate which is similar to the square Fe_2N monolayer on the Cu(001) substrate. From the X-ray photoelectron spectroscopy (XPS) and low energy electron diffraction (LEED), we found that the lattice of the Fe_2N monolayer was distorted toward a monoclinic lattice.

By changing the symmetry of the substrates, the electronic and magnetic properties of the square Fe_2N monolayer can be tuned. The XAS/XMCD measurement reveals that the spin magnetic moment of the Fe_2N monolayer on the Cu(111) substrate became less than half of that of the Cu(001) substrate. From the dI/dV spectra, we consider that this is attributed to the difference in the local hybridization.

Next, we have fabricated the Co-mixed iron nitride layer on the Cu(001) substrate. The magnetic moment of this Co-mixed iron nitride film estimated by XAS/XMCD increased compared with the Fe_2N monolayer. the local density of states became similar to that of the γ'-Fe_4N trilayer with the strong spin magnetic moment. The Co atoms enhance the spin magnetic moment of the iron nitride layer.

Finally, we have fabricated a new hexagonal iron nitride film on the Cu(111) substrate by changing the sample preparation procedure. The structure was very similar to the iron nitride film on the Cu(001) substrate. We observed

the strong peak at the positive bias voltage which is not observed in other iron nitride films.

In our dissertation, we found that hexagonal iron nitride monolayer and square one are selectively fabricated on the Cu(111) substrates by changing the fabrication condition. In addition, we discovered that the magnetic moment of the square Fe_2N monolayer is controlled by selecting the layer under the Fe_2N monolayer.

Contents

Chapter 1

Introduction

1.1 Preface

The history of magnetism is traced back to 5000 years ago. Greek found that iron is attracted by a rock containing Fe_3O_4. According to one account, the word "magnet" is named after the province of Magnesia where the rock was found for the first time [1]. The first practical use of magnets was a compass. It was used for the navigation in the age of discovery. In the 20th century, the demand for the magnetic materials was increased since the magnets were used as a motor, a generator and so on at that time. People began to search for the permanent magnet with the high coercivity [2]. After the KS steel containing Co, W, and Cr was artificially synthesized by K. Honda *et al.*, in 1920 [3], many permanent magnet such as alnico and ferrite were discovered. In particular, the neodymium magnet $Nd_2Fe_{14}B$ discovered in 1984 [4] has been widely used because of the large saturation magnetization and the high crystal magnetic anisotropy. Nowadays, the magnetic materials are widely utilized in our daily lives such as hard desk drive, mobile phone and so on. In addition, in step with the development of the spintronics, the materials with small saturation magnetization also begin to draw attention [5, 6].

Iron nitrides have attracted much attention as a ferromagnetic material because of their various electronic and magnetic properties depending on the N content and structure [7–10]. There are various phases of α''-$Fe_{16}N_2$, γ'-Fe_4N, ϵ-Fe_3N, and ζ-Fe_2N. They are fabricated by heating Fe under NH_3/H_2 gas. In particular, the large saturation magnetization in α''-$Fe_{16}N_2$ higher than α-Fe reported by T. K. Kim *et al.*, [11] inspired various research related to the magnetic materials [12, 13]. Y. Takahashi *et al.*, reported that an Fe_2N monolayer film corresponding to a plane of γ'-Fe_4N grows on the Cu(001) substrate and it exhibits ferromagnetism with the spin magnetic moment of 1.1 μ_B/atom [14, 15]. Recently, the hexagonal iron nitride monolayer are also

observed near the step edge of the Cu(001) substrates by the other fabrication procedure [16].

The monolayers are distorted by the substrates and the distance between the atoms is changed. In addition, the charge transfer from the substrates affects the density of states of iron nitride layers. These effects by the substrates change the electronic and magnetic properties of the monolayers [17]. In order to elucidate the origin of the magnetic properties induced by the substrates, the iron nitride monolayer is one of the appropriate materials since the robust in-plane bonding between Fe and N atoms prevents from mixing at the interface. However, iron nitride monolayers are observed only on the Cu(001) substrate so far. Firstly, we have to fabricate the iron nitride monolayers on other substrates. It is expected that several stable phases are observed on other substrates by controlling fabrication procedure as seen in the Cu(001) substrate [15, 16]. Investigating the magnetic properties of iron nitride monolayers could lead to elucidate the way to fabricate the iron nitride films with the large magnetic moment like α''-$Fe_{16}N_2$.

1.2 Purpose of study

In this dissertation, we have investigated how the magnetic properties of iron nitride monolayers are affected by the layers under the monolayers. In order to achieve our goal, first of all, we have discovered the growth condition of the new iron nitride monolayers on several substrates. After that, we have investigated their electronic and magnetic properties.

For this study, we have conducted the atomic scale observation for the surface morphology and local density of states by using the scanning tunnel microscopy/spectroscopy (STM/STS). STM is an useful method to measure the growth condition since STM enables us to observe the surface morphology directly with considering the surface roughness and atomic-scale defects. The magnetic properties were investigated by using XAS/XMCD measurements. We can obtain element specific information on the magnetic properties quantitatively.

1.3 Outline

Our dissertation consists of eight chapters as below:

In Chapter 2, we firstly introduce the principle of the experimental techniques we used in our dissertation. Then, we summarize the previous research of iron nitride.

In Chapter 3, we explain our experimental system and our sample preparation method.

In Chapter 4, we report the growth and structure of iron nitride monolayers on the Cu(111) substrate. The square Fe_2N monolayer similar to that on the Cu(001) substrate is fabricated. We propose the structure model of the Fe_2N monolayer on the Cu(111) substrate.

In Chapter 5, we compare the electronic and magnetic properties of the square Fe_2N monolayer on the Cu(111) substrate with those on the Cu(001) substrate. We presents the result of the electronic and magnetic properties of the square Fe_2N monolayer induced by the substrates.

In Chapter 6, we show the Co-mixed iron nitride films on the Cu(001) substrates fabricated by codepositing Co and Fe. We observed Fe and Co layers are fabricated under the Fe_2N monolayer. We describe the magnetic properties of the films investigated by using XAS/XMCD.

In Chapter 7, we show the structure of the new hexagonal iron nitride monolayer on the Cu(111) substrate. we discuss the growth condition and the structure.

Finally, we summarize and conclude our dissertation in Chapter 8.

Chapter 2

Experimental method

2.1 Scanning tunnel microscopy

Scanning tunnel microscopy (STM) is a technique for observing the surface morphology at the atomic level by using an atomically-sharp tip. It detects the tunneling current between the sample and the tip. Figure 2.1 shows the STM image of the clean Cu(111) substrate with the atomic resolution. STM has been widely used since the first STM observation by G. Binnig and H. Rohrer in 1982 [18].

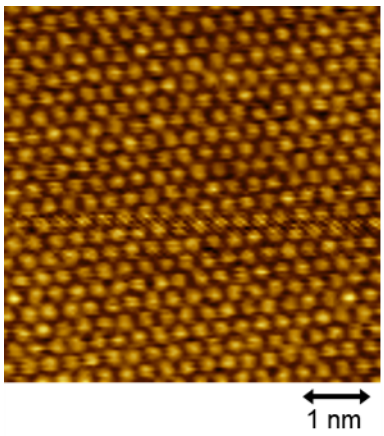

Figure 2.1: Atomically-resolved topographic STM image of the clean Cu(111) substrate.

We describe the principle of STM by using a one-dimensional rectangular potential model shown in Fig. 2.2 (a). The region 1 and region 3 shown in Fig. 2.2 (a) indicate a sample region and a tip region respectively. The region 2 describes the vacuum region between the sample and the tip with the energy barrier V. In the classical model, the electron in the region 1 with

the energy E ($\leq V$) cannot overcome the energy barrier in the region 2. It, however, can pass the barrier by the tunneling effect in the quantum system. A Schorödinger's equation of this one dimensional model can be described as below:

$$[-\frac{\hbar^2}{2m}\frac{\partial^2}{\partial z^2} + V(z) - E]\Psi = 0, \tag{2.1}$$

$$\text{for} \quad V(z) = \begin{cases} 0 & \text{(region 1,3)} \\ V & \text{(region 2)} \end{cases}$$

where m is the mass of the electron, Ψ the wave function of the electron, $\hbar$ the Dirac's constant. The differential equation of Eq. (2.1) is solved as

$$\begin{aligned} &\text{region 1 } (z < 0) \\ &\Psi = \mathrm{A}e^{ikz} + \mathrm{B}e^{-ikz} \\ &k = \frac{\sqrt{2mE}}{\hbar} \\ &\text{region 2 } (0 < z < a) \\ &\Psi = \mathrm{C}e^{\kappa z} + \mathrm{D}e^{-\kappa z} \\ &\kappa = \frac{\sqrt{2m(V-E)}}{\hbar} \\ &\text{region 3 } (a < z) \\ &\Psi = \mathrm{F}e^{ikz} \\ &k = \frac{\sqrt{2mE}}{\hbar} \end{aligned} \tag{2.2}$$

where A, B, C, D and F are normalization constants. The wave function Ψ and its differential function $d\Psi/dz$ must be the continuous function at the boundary. Therefore, the transmittance T is obtained as

$$T = \frac{|\mathrm{F}|^2}{|\mathrm{A}|^2} = \frac{1}{1 + \frac{4k^2\kappa^2}{(k^2+\kappa^2)^2}\sinh^2(\kappa a)} \tag{2.3}$$

The tip-sample distance a is usually much larger than the wavelength $1/\kappa$, *i.e.* $\kappa a \gg 1$. In this approximation, the transmittance T is given by

$$\begin{aligned} T &= \frac{16k^2\kappa^2}{(k^2+\kappa^2)^2}e^{-2\kappa a} \\ \kappa &= \frac{\sqrt{2m(V-E)}}{\hbar} \end{aligned} \tag{2.4}$$

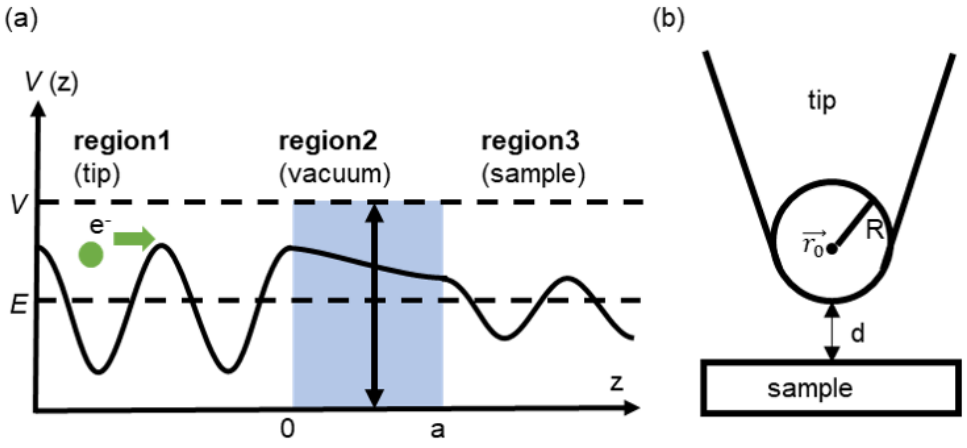

Figure 2.2: (a) One dimensional rectangular potential model. In this model, the electron moving from the region 1 to the region 3 is considered. (b) Schematic image of Tersoff and Hamann model [19]. The wave function of the tip is assumed to be a s-like wave function. The distance between the tip and the sample is d. The radius of a curvature of the tip is R. The center of the curvature is $\vec{r_0}$.

Equation 2.4 means that the tunneling current which is proportional to the transmittance T varies exponentially with the tip-sample distance a. In the actual system, the tunneling current increases by one order of magnitude per 0.1 nm.

The tunneling current does not only depend on the tip-sample distance, but also on the local density of states. When applying the voltage V, the current I_{ts} flowing from the tip to the sample is written as

$$I_{ts} = e \int \rho_t(E)\rho_s(E - eV)T(E, V)dE \tag{2.5}$$

where ρ is the density of state and T the transmittance. The subscripts 's' and 't' mean a sample and a tip respectively. Here, we neglect the temperature dependence. According to the Fermi's golden rule, the transmittance T of the initial state $\mid i >$ to the final state $\mid f >$ is

$$T = 2\frac{\pi}{\hbar}|M_{fi}|^2\delta(E_f - E_i) \tag{2.6}$$

where M_{fi} is the matrix element from the initial state to the final state. Equation 2.6 indicates that the energy of the initial state E_i and that of the final state E_f must be the same. Equation (2.5) denotes the current generated by the electrons moving from an occupied state of the tip (ρ_t) to the unoccupied

state of a sample (ρ_s). By substituting Eq. (2.6) into Eq. (2.5), one obtains

$$I_{ts} = \frac{2\pi e}{\hbar} \int \rho_t(E)\rho_s(E - eV) \times |M_{ts}|^2 dE \tag{2.7}$$

At the low bias voltage, Eq. (2.7) can be written as

$$I = \frac{2\pi}{\hbar} e^2 V \sum_{s,t} |M_{ts}|^2 \delta(E_s - E_\mathrm{F}) \delta(E_t - E_\mathrm{F}) \tag{2.8}$$

where E_F is Fermi energy. Here, we consider the matrix element M_{ts}. J. Bardeen suggests that M_{ts} is given by [20]

$$M_{ts} = \frac{\hbar^2}{2m} \int d\vec{S} \cdot (\Psi_t^* \vec{\nabla} \Psi_s - \Psi_s^* \vec{\nabla} \Psi_t) \tag{2.9}$$

We choose the wave functions of the surface Ψ_s as below [19]

$$\Psi_s = \sum_{\vec{G}} a_{\vec{G}} e^{\sqrt{(\kappa^2 + |\vec{k_{||}} + \vec{G}|^2} z} e^{i(\vec{k_{||}} + \vec{G}) \cdot \vec{x}} \tag{2.10}$$

where $\vec{k_{||}}$ is the surface Bloch vector, $\vec{G}$ the surface reciprocal lattice vector, and κ is given as $\frac{\sqrt{2mW}}{\hbar}$ (W: work function). The wave function in Eq. (2.10) varies periodically at the direction parallel to the surface and it decays with the decay length of $1/\kappa$ at the normal direction to the surface. The wave function of the tip Ψ_t is simply assumed to be a s-wave function and to be localized within a radius of R as shown in Fig. 2.2 (b). The wave function of the tip is written as

$$\Psi_t = \mathrm{C} k R e^{kR} \frac{1}{(k|\vec{r} - \vec{r_0}|)} e^{-k|\vec{r} - \vec{r_0}|} \tag{2.11}$$

where C is a normalized constant. The relation between R and $\vec{r_0}$ is shown in Fig. 2.2 (b). Since the matrix element is strongly dependent on the overlap of the wave functions of the tip with that of the sample, the wave function of the sample at the nearest area from the tip impacts on the tunneling current. By substituting the wave functions of Eq. (2.10) and Eq. (2.11) to Eq. (2.9), one obtains [19]

$$M_{ts} \propto k R e^{kR} \Psi_s(\vec{r_0}) \tag{2.12}$$

Therefore, the tunneling current is

$$I \propto \rho_s(E_\mathrm{F}) \sum_s |\Psi_s(r_0)|^2 \delta(E_s - E_\mathrm{F}) \tag{2.13}$$

It suggests that we can observe the local density of states near the E_F by STM.

The voltage dependency on dI/dV can be written by using Eq. (2.5) [21]

$$\frac{dI}{dV} \propto e\rho_s(E_\mathrm{F}+eV)T(E_\mathrm{F}+eV,V) + \int_{E_\mathrm{F}}^{E_\mathrm{F}+eV} \frac{d}{dV}[\rho_s(E)T(E,V)]dE \quad (2.14)$$

The first term is proportional to the local density of states of the sample at the applied voltage. The second one is a background term which arises from the transmittance parameter or differential local density of states of the tip. Since the transmittance is nearly independent on the bias voltage, the second term can be neglected. Thus, Equation 2.14 is written as

$$\frac{dI}{dV} \propto e\rho_s(E_\mathrm{F}+eV)T(E_\mathrm{F}+eV,V) \quad (2.15)$$

sometimes $(dI/dV)/(I/V)$ are used instead of dI/dV to reduce the background.

$$\frac{\frac{dI}{dV}}{\frac{I}{V}} = \frac{\rho_s(eV)\rho_t(0) + \int_0^{eV} dE \frac{\rho_s(E)\rho_t(-eV+E)}{eT(eV,V)} \frac{dT(E,eV)}{dV}}{\frac{1}{eV}\int_0^{eV} dE\rho_s(E)\rho_t(-eV+E)\frac{T(E,eV)}{T(eV)}} \quad (2.16)$$

2.2 X-ray photoemission spectroscopy

The X-ray photoemission spectroscopy (XPS) is a surface sensitive technique and is intensively used to investigate the chemical binding energy and the elemental composition qualitatively. The electrons in the core level are excited by the X-ray with the photon energy of $h\nu$ and subsequently is emitted to a vacuum. This phenomenon is described as

$$E_\mathrm{K} = h\nu - E_\mathrm{B} - W \quad (2.17)$$

where E_K is the kinetic energy of the electron, E_B the binding energy and W work function. The binding energy is estimated from Eq. (2.17) by measuring the kinetic energy of the photoelectron by using hemisphere analyzer.

Some photoelectrons excited by the X-ray lose their energy by the inelastic or elastic scattering with phonon, impurity, and defect states. Since the typical electron escape depth is around 1 nm at photon energy of 100 eV, the XPS method is regarded as the surface sensitive method. The Al Kα X-ray and Mg Kα X-ray are usually used as X-ray sources. The photon energies of Al Kα X-ray and Mg Kα are 1486.6 eV and 1253.6 eV respectively. The XP spectrum of the clean Cu(111) substrate is displayed in Fig. 2.4.

The peak position of the binding energy is shifted by several effects. For example, the binding energy of the oxides is much higher than that of the single element since oxygen has a large electronegativity. This is called as chemical shifts. As increasing the ionic valence, the binding energy becomes

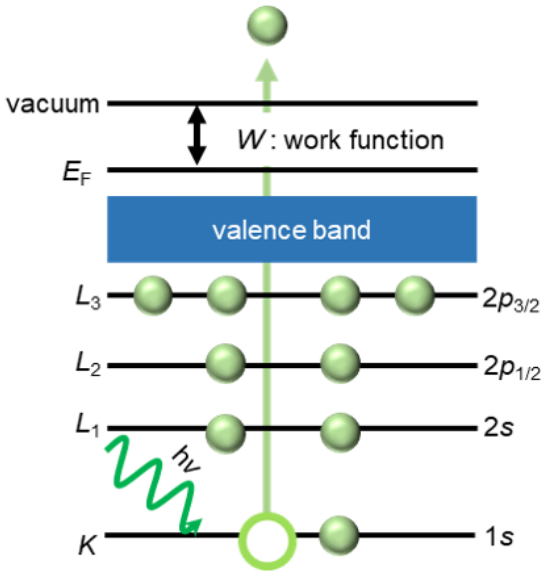

Figure 2.3: Schematic image of the principle for XPS.

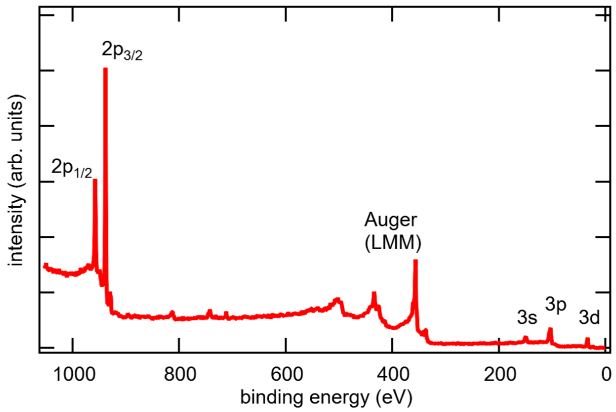

Figure 2.4: XP spectrum of the clean Cu(111) substrate.

higher. Therefore, the XPS studies are also used to measure the ionic valence of the elements.

The inelastic scattering induced by the photoelectrons makes the background of XPS. It is necessary to subtract the background in order to analyze the spectra quantitatively. There are several ways to subtract the background. One of the simplest ways is to draw the straight line from the pre-edge to the post-edge. However, this method is very difficult to estimate the peak area quantitatively since the post edge position strongly affects the peak area.

Here, we introduce the one conventional way called as the Shirley method [22]. One assumes that the number of the inelastic electron is proportional to

the peak intensity of XPS and that it is independent on the energy loss.

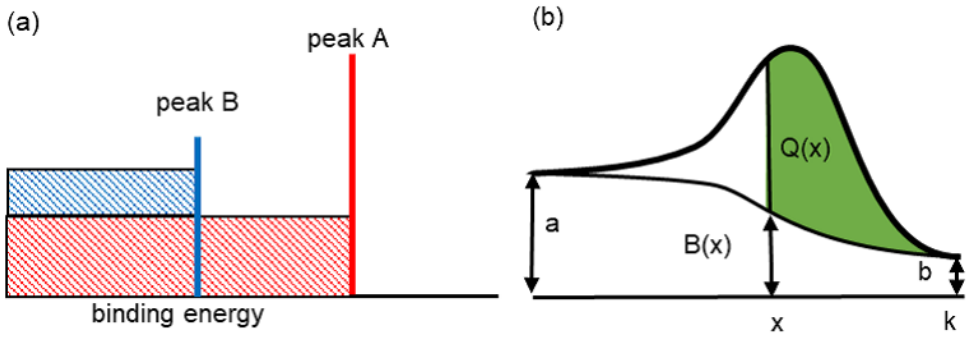

Figure 2.5: (a) Delta peak and the background proportional to the intensity of the delta peaks. (b) Schematic image of the Shirley method.

Figure 2.5 (a) describes the background of the delta-like peaks estimated by the Shirley method. The background proportional to the peak intensities of the delta-like peaks is generated at the higher binding energy. Here, the background $B(x)$ at the binding energy x can be written as

$$B_i(x) = (a - b)\frac{Q_i(x)}{T_i} + b \tag{2.18}$$

where T_i is the total peak area after subtracting the background, $Q_i(x)$ the peak area from the pre-edge energy to the energy x, a and b the intensities at the post-edge and the pre-edge. The background is calculated as follows: 1) The constant background b which is the same intensity as that at the pre-edge is subtracted. 2) Assuming $B_{i=0}(x) = b$, one calculates the peak intensity $Q_{i=0}(x)$ and $T_{i=0}$ from the spectra. 3) The background $B_{i=1}(x)$ is calculated by substituting $Q_{i=0}(x)$ and $T_{i=0}(x)$ to Eq. (2.18). 4) Repeating the cycle of 2) and 3) until $Q_i(x)$ and T_i converge. Here, i denotes the number of cycles of these processes.

The careful measurement of XPS allows us to estimate the chemical composition quantitatively. The number of the photoelectrons M generated by XPS is written as

$$M = I_0 N \sigma \tag{2.19}$$

where I_0 is X-rays intensity, N number of atoms in a unit area, and σ ionic cross section.

Here, we introduce the relative sensitivity factor S_i of element i. It is defined as

$$S_i = \frac{I_{i,\mathrm{ref}}}{I_{\mathrm{ref}}} \tag{2.20}$$

$I_{i,\mathrm{ref}}$ is the intensity of the reference sample of the element i and I_{ref} is that of the reference materials. The $1s$ peak of fluorine in lithium fluoride is used as the reference material. Relative sensitive factors of all elements are obtained by measuring the photoelectron intensity of all elements. The concentration of the unknown material X_i of the element i is obtained by using relative sensitive factor as

$$X_i = \frac{I_i}{I_{\mathrm{ref}} S_i} \tag{2.21}$$

where I_i is the XPS intensity of the unknown materials of the element i. By measuring all elements in the unknown materials, we can obtain the normalized concentration of the unknown materials as below:

$$X_i = \frac{\frac{I_i}{I_{\mathrm{ref}} S_i}}{\sum^n \frac{I_j}{I_{\mathrm{ref}} S_j}} = \frac{\frac{I_i}{S_i}}{\sum^n \frac{I_j}{S_j}} \tag{2.22}$$

2.3 X-ray absorption spectroscopy/ X-ray magnetic circular dichroism

X-ray absorption spectroscopy/X-ray magnetic circular dichroism (XAS/XMCD) is a surface sensitive method to measure the magnetic properties quantitatively. The XA spectra is an absorption spectra from the inner occupied state to the outer unoccupied states by irradiating X-ray. Here, we consider the transition from the occupied states $\mid l, m >$ to the unoccupied states $\mid l', m' >$. The l and m denotes the orbital angular momentum and the spin angular momentum. They obey the equations as below.

$$\begin{aligned} l' - l &= \pm 1 \\ m' - m &= \eta \end{aligned} \tag{2.23}$$

In the case of the transition induced by the liner polarized light, η should be 0. In contrast, in the case of the transition induced by the circularly polarized light, η should be ± 1. Equation (2.23) is called as selection rule.

XMCD is defined as the difference between the absorption of right- and left-handed circularly polarized light. When the same number of d electrons are occupied both in the spin-up band and spin-down band, *i.e.* spin polarization is zero, the transition rate from spin-up (spin-down) band by the right(left)-handed circularly polarized light is the same as that from the spin-down (spin-up) band by the left (right)-handed circularly polarized light. The XA spectra obtained by the right-handed circularly polarized light is the same intensity as that obtained by the left-handed circularly polarized light. Therefore, no XMCD signal is obtained if the paramagnetic materials or non-spin polarized

materials are measured. In the case of the ferromagnetic materials, the number of the electrons in the spin-up band is different from that in the spin-down band due to the exchange splitting. The XA spectra of the ferromagnetic materials obtained by the right-handed circularly polarized light is different from by the left-handed circularly polarized light. Therefore, one can obtain the XMCD signal. Since the absorption energy is different in each material, we can obtain the magnetic properties for each element.

B. T. Thole *et al.*, [23] and P. Carra *et al.*, [24] suggest that the spin magnetic moment and orbital moment are estimated from the experimental XAS/XMCD measurements quantitatively. Here, we define three parameters as below.

$$p = \int_{L_3} (\mu_+ - \mu_-) dE \tag{2.24a}$$

$$q = \int_{L_3+L_2} (\mu_+ - \mu_-) dE \tag{2.24b}$$

$$r = \int_{L_3+L_2} (\mu_+ + \mu_- - b.g.) dE \tag{2.24c}$$

where μ_+ (μ_-) is the XA spectra obtained by right-handed (left-handed) circularly polarized light, $b.g.$ means the background. The relation between these three parameters and the spectra is shown in Fig. 2.6. The spin magnetic moment $\langle S_z \rangle$ and the orbital magnetic moment $\langle L_z \rangle$ of $3d$ orbital are written as [23, 24]

$$\langle S_z \rangle + \frac{7}{2} \langle T_z \rangle = -\frac{6p - 4q}{r} (10 - n_{3d}) \tag{2.25}$$

$$\langle L_z \rangle = -\frac{4q}{3r} (10 - n_{3d}) \tag{2.26}$$

where $\langle T_z \rangle$ is the magnetic dipole operator and n_{3d} the number of the $3d$ electrons. These are called as sum rule. The value of $\langle T_z \rangle$ can be often ignored since it is usually much less than that of $\langle S_z \rangle$.

2.4 Low energy electron diffraction

Low energy electron diffraction (LEED) is a surface-sensitive method for investigating the surface structure. The electron with the incidence energy of 30 - 300 eV is irradiated to the sample vertically. The two dimensional reciprocal lattice pattern is obtained by observing the backscattering electron by the hemisphere screen. Since the electron escape depth is less than 2 nm which is much lower than X-ray penetration depth, LEED has widely been used to measure the surface structure. According to the de Broglie wave, the

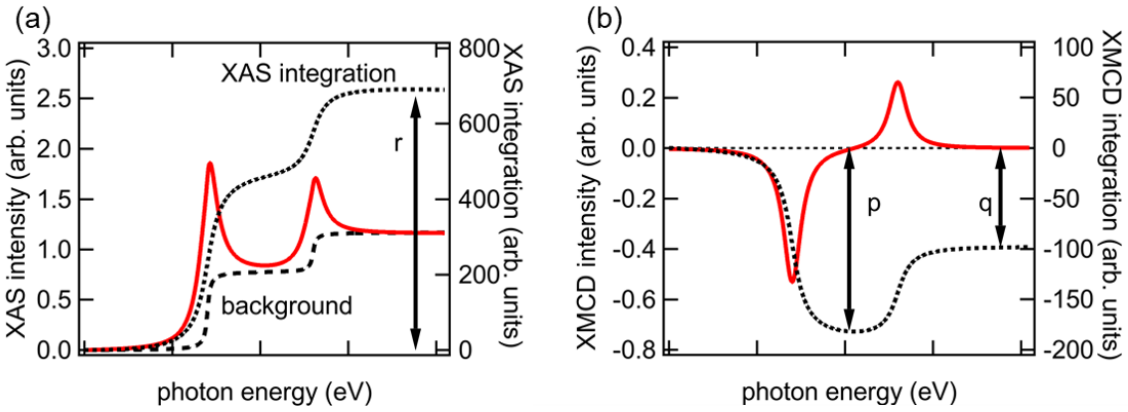

Figure 2.6: XA spectra and XMCD spectra generated by some Lorentzian functions. The values p, q, and r correspond to Eq. (2.24a)-Eq. (2.24c)

wavelength of the electron λ and kinetic energy E_{K} are written as

$$\lambda = \frac{h}{p} \tag{2.27}$$

$$E_{\mathrm{K}} = \frac{p^2}{2m} \tag{2.28}$$

where h is the Planck constant, p the momentum of the electron, and m the mass of the electron. From these equations, one obtains

$$\lambda = \frac{h}{\sqrt{2mE_{\mathrm{K}}}} \approx \sqrt{\frac{1.504}{E_{\mathrm{K}}}}(\mathrm{nm}) \tag{2.29}$$

The wavelength of the electron with the incidence energy of a few hundred eV is estimated to be approximately 1 Å which is almost the same as the lattice constant of the sample. Therefore, the diffraction pattern is obtained by using electron instead of X-ray.

We consider a crystal which is defined as three vectors $\boldsymbol{a}_1$, $\boldsymbol{a}_2$, and $\boldsymbol{a}_3$. Here, $\boldsymbol{a}_1$ and $\boldsymbol{a}_2$ are unit cell vectors parallel to the surface and $\boldsymbol{a}_3$ is normal to the surface. The scattering intensity F is written as

$$F = \frac{\sin^2(\frac{N_1}{2}\boldsymbol{a}_1\Delta\boldsymbol{k})}{\sin^2(\frac{1}{2}\boldsymbol{a}_1\Delta\boldsymbol{k})}\frac{\sin^2(\frac{N_2}{2}\boldsymbol{a}_2\Delta\boldsymbol{k})}{\sin^2(\frac{1}{2}\boldsymbol{a}_2\Delta\boldsymbol{k})}\frac{\sin^2(\frac{N_3}{2}\boldsymbol{a}_3\Delta\boldsymbol{k})}{\sin^2(\frac{1}{2}\boldsymbol{a}_3\Delta\boldsymbol{k})} \tag{2.30}$$

$$\Delta\boldsymbol{k} = \boldsymbol{k}_f - \boldsymbol{k}_i \tag{2.31}$$

where $\boldsymbol{k}_i$ is the wave vector of the incidence wave, $\boldsymbol{k}_f$ the wave vector of the scattering wave and N_i (i=1, 2, 3) the number of atoms along $\boldsymbol{a}_i$. Equation 2.30 has peaks when the following equations are obeyed.

$$\boldsymbol{a}_1\Delta\boldsymbol{k} = 2\pi l, \boldsymbol{a}_2\Delta\boldsymbol{k} = 2\pi m, \boldsymbol{a}_3\Delta\boldsymbol{k} = 2\pi n \tag{2.32}$$

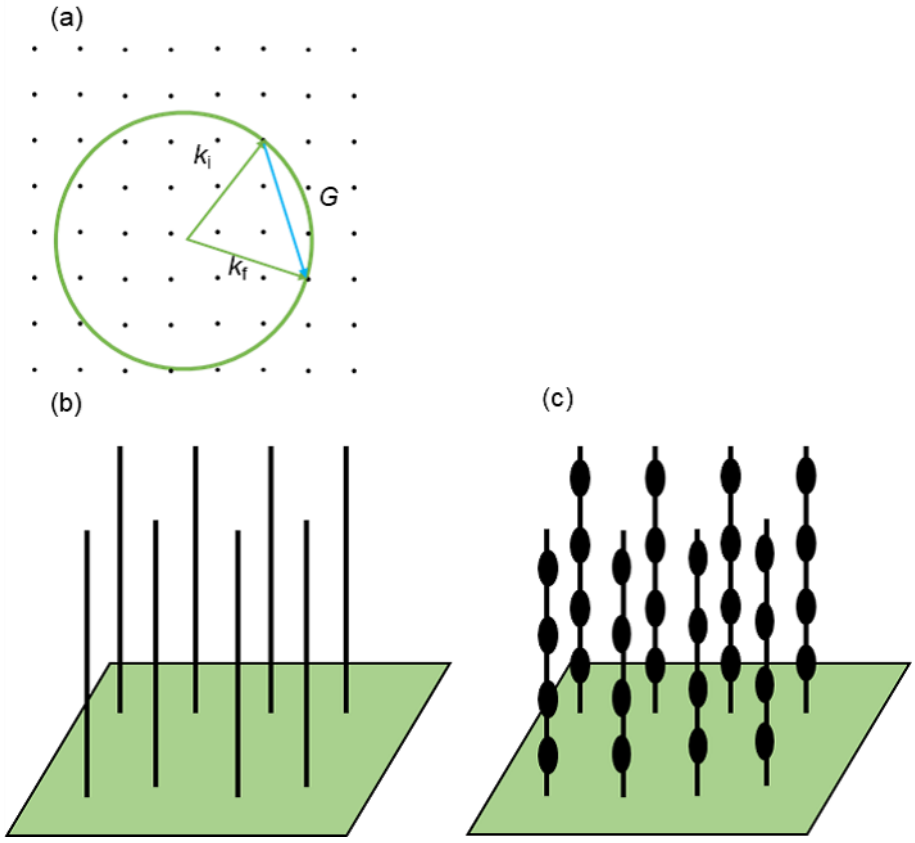

Figure 2.7: (a) Reciprocal vector point group and the Ewald sphere with the radius of $|\boldsymbol{k}_f|$. (b) Reciprocal 'rod' in the case of the N_3 =1. (c) Reciprocal 'rod' in the case of the actual LEED pattern.

where l, m, and n are integer. We can define the vector $\boldsymbol{G}$ which obeys Eq. (2.32) as

$$\boldsymbol{G} = \Delta\boldsymbol{k} = l\boldsymbol{b}_1 + m\boldsymbol{b}_2 + n\boldsymbol{b}_3 \tag{2.33}$$

The $\boldsymbol{b}_i$ (i = 1, 2, 3) is defined as

$$\boldsymbol{b}_1 = 2\pi\frac{\boldsymbol{a}_2 \times \boldsymbol{a}_3}{\boldsymbol{a}_1 \cdot (\boldsymbol{a}_2 \times \boldsymbol{a}_3)}, \boldsymbol{b}_2 = 2\pi\frac{\boldsymbol{a}_3 \times \boldsymbol{a}_1}{\boldsymbol{a}_1 \cdot (\boldsymbol{a}_2 \times \boldsymbol{a}_3)}, \boldsymbol{b}_3 = 2\pi\frac{\boldsymbol{a}_1 \times \boldsymbol{a}_2}{\boldsymbol{a}_1 \cdot (\boldsymbol{a}_2 \times \boldsymbol{a}_3)} \tag{2.34}$$

In addition, we assume that the electron does not lose energy during the scattering,

$$|\boldsymbol{k}_i| = |\boldsymbol{k}_f| \tag{2.35}$$

When the scattering vector $\boldsymbol{k}_f$ obeys Eq. (2.33) and Eq. (2.35), the intensity of the diffraction is maximum. The vector $\boldsymbol{G}$ is called as a reciprocal vector.

Here, we seek the scattering vector $\boldsymbol{k}_f$ by using the Ewald sphere. Figure 2.7 (a) shows the reciprocal vector point group. For simplicity, we consider only two dimension vector. Here, the end point of $\boldsymbol{k}_i$ is fixed at a reciprocal vector point. Then, we draw a sphere which obeys two conditions; 1) The center of the sphere is located at the start point of $\boldsymbol{k}_i$. 2) The radius of the sphere is equal to $|\boldsymbol{k}_f|$. When the sphere overlaps the reciprocal vector point group, we obtain the scattering vector $\boldsymbol{k}_f$ which satisfies Eq. (2.33) and Eq. (2.35) as shown in Fig. 2.7 (a). This sphere is called as an Ewald sphere.

When one assumes that all electrons are scattered at the top layer, *i.e.* $N_3 = 1$ in Eq. (2.30), the term $\frac{\sin^2(\frac{N_3}{2}\boldsymbol{a}_3\Delta\boldsymbol{k})}{\sin^2(\frac{1}{2}\boldsymbol{a}_3\Delta\boldsymbol{k})}$ is always 1, and the reciprocal vector point group is a 'rod' along the normal direction to the surface as shown in Fig. 2.7 (b). In this case, the Ewald sphere always overlaps the rods. Therefore, the two dimensional patten by LEED is observed irrespective of the incidence energy. In the case of the actual LEED pattern, the electrons are scattered from a few layers depth. Then, the 'rod' becomes like Fig. 2.7 (c). Therefore, the peak intensity gradually changes with increasing the incidence energy.

2.5 Moiré pattern

Moiré pattern appears when superposing two sets of lines. Figure 2.8 shows examples of moiré pattern formed by overlapping geometrical patterns. Here, we theoretically calculate the gap and angle of the moiré pattern obtained by using the two stripe pattern shown in Fig. 2.9.

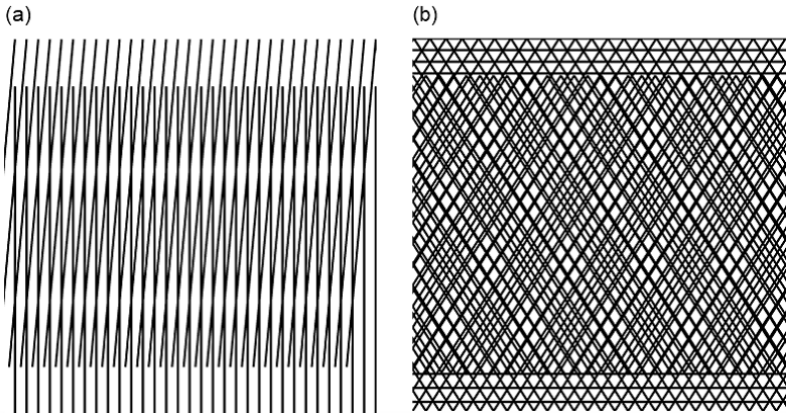

Figure 2.8: Moiré pattern formed by simple lines: (a) Two sets of lines with different direction, (b)Two sets of hexagonal patterns with different steps.

Here, we define the step of the first line pattern as a, that of the second one as b and the angle between two line patterns as θ. We consider that the

first pattern is parallel to the y axis.

$$x = na \ (n = 0, \pm 1, \pm 2, \pm 3, \cdots) \tag{2.36}$$

The second pattern in Fig. 2.9 can be described by using the angle θ.

$$y = \frac{1}{\tan\theta} x - \frac{mb}{\sin\theta} \ (m = 0, \pm 1, \pm 2, \pm 3, \cdots) \tag{2.37}$$

In addition, n and m satisfy

$$n - m = p \ (p = 0, \pm 1, \pm 2, \pm 3, \cdots) \tag{2.38}$$

By eliminating n and m from Eq. (2.36) - Eq. (2.38), one obtains the equation of moiré pattern.

$$y = \frac{a\cos\theta - b}{a\sin\theta} - p\frac{a}{\sin\theta} \tag{2.39}$$

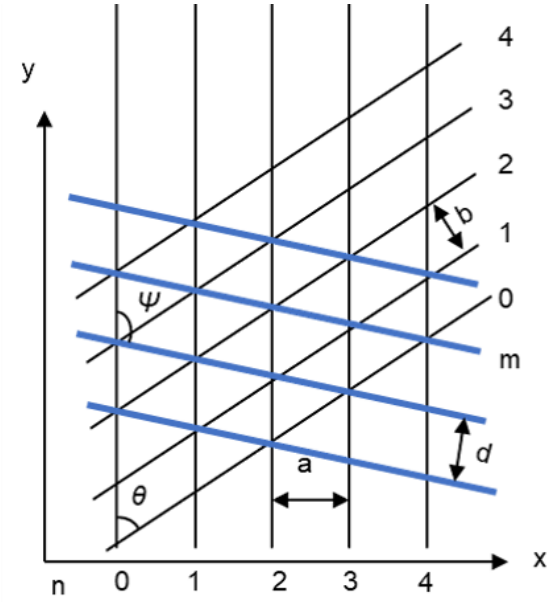

Figure 2.9: Moiré pattern formed by simple lines. The two sets of black lines form the moiré pattern as indicated by blue lines.

In addition, by using the step of the moiré pattern d and the angle between the first line pattern and the moiré pattern ψ, the equation of moiré pattern is also written as

$$y = \frac{1}{\tan\psi} x - p\frac{d}{\sin\psi} \tag{2.40}$$

The coefficients of Eq. (2.39) and Eq. (2.40) should be equal. Therefore, one obtains

$$d = \frac{ab}{\sqrt{a^2 + b^2 - 2ab\cos\theta}} \tag{2.41}$$

$$\sin\psi = \frac{b\sin\theta}{\sqrt{a^2 + b^2 - 2ab\cos\theta}} \tag{2.42}$$

2.6 Iron nitride

Iron nitride attracted much attention because of a catalyst for a synthesis of ammonia in 1930s. F. Haber and C. Bosch discovered the ammonia synthesis way from N_2 gas and H_2 gas by using Fe catalysts under high pressure and high temperature in 1910s [28]. While the iron nitride is fabricated by this synthesis way, it suppresses the ammonia synthesis. Therefore, it was necessary to determine the dissociation condition of iron nitride in order to enhance the efficiency of the Fe catalysts [29, 30].

In 1940s, various phases of iron nitride, for example, γ'-Fe_4N and ϵ-Fe_3N were discovered. In particular, K. H. Jack greatly contributed to the structure determination for iron nitrides by using XRD [31–33]. Later, the magnetic properties of iron nitrides were investigated, and it was revealed that the iron nitrides exhibit ferromagnetism with a strong magnetic moment comparable to bcc α-Fe. Figure 2.10 (a) shows the phase diagram of Fe - N system [26]. There are various crystal structures of iron nitride depending on the N content. We introduce each structure and magnetic property.

α'' -$Fe_{16}N_2$, the Fe-richest phase, exhibits high saturated magnetization. In 1951, the α''-$Fe_{16}N_2$ was fabricated by K. H. Jack for the first time by annealing the nitrogen-martensite at 120 degree for 7 days [32]. However, the limited N solubility in Fe of less than 10.5 at/% indicates that the high-quality α''-$Fe_{16}N_2$ is not fabricated by the annealing. It is pointed out that other phases such as α-Fe (bcc) and γ'-Fe_4N were mixed [10]. In 1972, T. K. Kim and M. Takahashi fabricated α''-$Fe_{16}N_2$ film by depositing Fe on a glass substrate under the N atmosphere. The experiments by using torque magnetometer and the ferromagnetic resonance method revealed that the magnetic moment of α''-$Fe_{16}N_2$ is 3.0 μ_B/atom. Since this result was reported, many groups have tried to fabricate α''-$Fe_{16}N_2$ and measured the magnetic moment. Although there are differences in the quality of the samples, the saturation magnetizations are 2.4 - 3.5 μ_B/atom which are higher than α-Fe [34, 35]. The α''-$Fe_{16}N_2$ is drawn attention from the view point of applications since the spin magnetic moment is just as high as that of a neodymium magnet and the α''-$Fe_{16}N_2$ is a rare-earth-free material.

$\gamma'-Fe_4N$, the second Fe richest phase has a cubic structure in which N

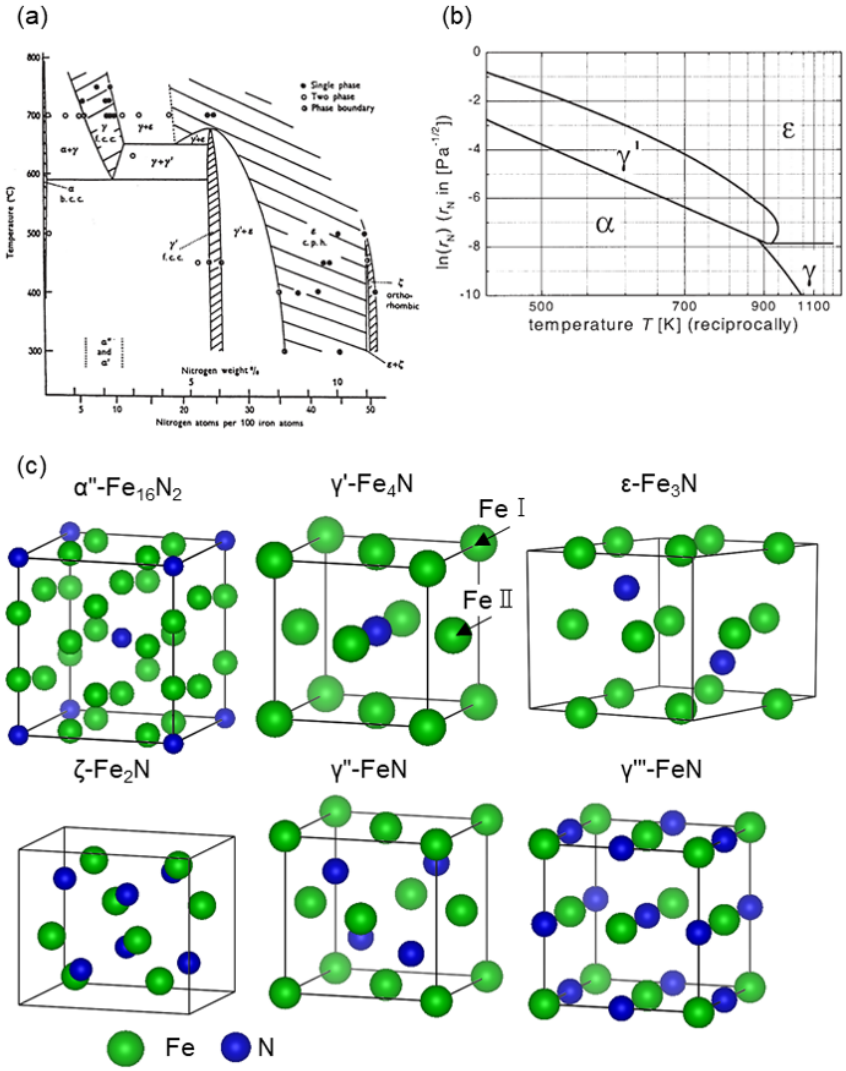

Figure 2.10: (a) Phase diagram of iron nitride system. (b) Lehrer diagram which is used as nitriding Fe in NH_3 and H_2 gas. The value r_N in the horizontal axis is defined as $P_{NH_3}/P_{H_2}^{3/2}$ by using the pressure of ammonia P_{NH_3} and hydrogen P_{H_2}. (c) Crystal structures of iron nitride depicted by VESTA [25] (a) : taken from Fig. 1 in [26], (b) : taken from Fig. 6 in [27]

atoms occupy the body center position of a fcc γ-Fe. While some structure models of Fe_4N were proposed at the early stage, its structure was determined from the polycrystalline samples by the X-ray diffraction (XRD) [31] and the neutron diffraction [36]. While these polycrystalline containing other phases were used to investigate the structures, the XRD measurements of the single phase of $\gamma'-Fe_4N$ later refined the lattice constants [37]. In the four Fe atoms in the unit cell, one Fe atom (FeI sites) is located at the corner position and is

surrounded by 12 neighbor Fe atoms. The other three Fe atoms (FeII sites) are located at the face center position with a bonding to two N atoms as described in Fig. 2.10 (c). The mössbauer study allows us to measure the site dependence on the spin magnetic moment of Fe [38, 39]. The spin magnetic moments of FeI sites and FeII sites are 3.0 μ_B/atom and 2.0 μ_B/atom respectively and the average magnetic moment per Fe atom of 2.2 μ_B/atom is comparable to Fe atoms [36]. The reported Curie temperature of $\gamma'-Fe_4N$ is 761 K [40] or 767 K [38].

ϵ-Fe_3N exhibits a hexagonal structure where N atoms are located at the hcp sites of the fcc γ-Fe. The lattice parameter of ϵ-Fe_3N measured by XRD is a = 470.80(6) pm, and c = 438.85(9) pm [37]. The spin magnetic moment of ϵ-Fe_3N is 1.9 μ_B/atom [8, 41] or 2.2 μ_B/atom [26]. The curie temperature investigated by neutron diffraction and superconducting quantum interference device (SQUID) is 575 K [26].

The octahedral sites of the fcc γ-Fe are randomly occupied by N atoms and $Fe_{2+x}N_1(0 \leq x \leq 1)$ are fabricated. As the N concentration increases, the Currie temperature and saturation magnetic moment decrease. The ideal structure ζ-Fe_2N exhibits very weak ferromagnetism and the Currie temperature is below 9 K [42]. The structure of ζ-Fe_2N is also determined by XRD [43].

One of the ways to fabricate the iron nitride is to anneal Fe under NH_3/H_2 atmosphere. According to Lehrer [27, 44], $\gamma'-Fe_4N$, ϵ-Fe_3N, and ζ-Fe_2N can be selectively fabricated by carefully controlling the temperature of Fe and the ratio of pressure of NH_3 to that of H_2. The phase diagram, called as Lehrer diagram is shown in Fig. 2.10 (b). However, the way to fabricate the single phase of α'' -$Fe_{16}N_2$ has not been discovered. It should be noted that all iron nitrides are metastable at room temperature compared with Fe and N_2 gas while this process is very slow at room temperature [8].

The theoretical calculation can explain the magnetic moment of the iron nitrides [7, 9]. By the N atom invasion to the Fe crystal, the volume of the crystal is expanded and the distance between Fe and Fe becomes longer, which localizes the density of states of Fe and increases the spin magnetic moment. In contrast, the N invasion impacts on the reduction of the spin magnetic moment of Fe since the electrons of Fe are delocalized by the strong hybridization between the N and Fe atoms. Therefore, at the low N content compounds, the former effect strongly affects the enhancement in the magnetic moment of iron nitrides. In contrast, at the N-rich compounds the latter effect strongly impacts on the reduction of the magnetic moment. As discussed above, the mössbauer study of γ'-Fe_4N revealed the site dependence on the magnetic moment. The volume expansion of γ'-Fe_4N compared with α-Fe affects the stronger magnetic moment of the FeI sites of γ'-Fe_4N than α-Fe. In contrast, the electrons of FeII sites are delocalized by the hybridization and the magnetic

moment of the FeII sites are smaller than α-Fe.

2.7 Iron nitride film

Iron nitride films are fabricated on various substrates. Especially, γ'-Fe_4N films are fabricated by molecular beam epitaxy (MBE) with Fe under the N atoms obtained from a radio frequency atomic source [10,45,46] or under NH_3 gas, by magnetron sputtering [47], and by nitriding Fe on the glass with flowing NH_3 and H_2 gas [48]. To best of our knowledge, only the MBE method achieves the single phase growth of the γ'-Fe_4N film. These films are relatively easily fabricated independent of the lattice mismatch between the substrates and the γ'-Fe_4N films. The γ'-Fe_4N films are fabricated on Cu(001) [10], $LaAlO_3$(001) [46, 49], $SrTiO_3$(001) [49], MgO(001) [45], NaCl(001) [47] and Si(001) [47].

The lattice mismatch between the γ'-Fe_4N and the substrate could enable us to tune the magnetic properties. The γ'-Fe_4N belongs to cubic crystal system and the lattice constant is $a = 374$ pm [9]. S. Atiq *et al.*, fabricate γ'-Fe_4N films on $LaAlO_3$(001) ($a = 379$ pm), $SrTiO_3$(001) ($a = 390$ pm), and MgO(001) ($a = 421$ pm). Here, a is a lattice constant [49]. While the saturation magnetization for γ'-Fe_4N on $LaAlO_3$(001) is 2.9 μ_B/atom, that on MgO(001) which causes the lattice mismatch between the film and the substrate is 2.6 μ_B/atom. The lattice mismatch between the films and the substrates can induce the lattice distortion to the film. The ϵ-Fe_3N films are fabricated on the AlN(0001)/3C-SiC/Si(111) [50], GaN(0002) [51] and $SrTiO_3$(001) [52]. However, the ϵ-Fe_3N films on GaN(0002) coexists the α-Fe and the single crystal fabrication is not achieved [51].

In addition to the spin magnetic moment, the spin polarization characterizes the magnetic properties. The spin polarization P(E) is defined as

$$P(E) = \frac{D_\uparrow(E) - D_\downarrow(E)}{D_\uparrow(E) + D_\downarrow(E)} \tag{2.43}$$

where $D_\uparrow(E)$ ($D_\downarrow(E)$) is the density of state of majority (minority) band at energy E. It is theoretically suggested that the spin polarization at the Fermi energy $P(E_F)$ of the $\gamma'-Fe_4N$, ϵ-Fe_3N and ζ-Fe_2N are 0.3, 0.5, and 0.7, respectively [9, 50]. Therefore, the ϵ-Fe_3N and ζ-Fe_2N films have potential to be used as a magnetic tunnel junction (MTJ) device [53]. In fact, fundamental research about α-Fe/AlN/ϵ-Fe_3N [54] and Cu_3N/Fe_4N [55] are conducted in order to fabricate the MTJ device by using iron nitride films.

The N-richer iron nitride phases, the $\gamma''-$FeN phase with a ZnS type structure and the $\gamma'''-$FeN phase with the NaCl type structure [56, 57] are grown by the DC sputtering. To best of our knowledge, they are not fabricated in the bulk system. The lattice constant of $\gamma''-$FeN is $a = 433$ pm and that of

$\gamma'''-$FeN is $a = 450$ pm by XRD [58]. The mössbauer measurements indicate that the ZnS type $\gamma''-$FeN exhibits nonmagnetism. In contrast, the mössbauer spectra of the sample including a NaCl type $\gamma'''-$FeN has two sextets spectrum. However, the peak broadening are not observed when increasing the applied magnetic field. It suggests that $\gamma'''-$FeN exhibits antiferromagnetism at 4 K [59].

The epitaxial growth succeeded only in growth of the $\gamma'''-$FeN phase on the GaN(0001) substrate [60] and on the Cu(001) substrate [61]. To best of our knowledge, it seems that there is no report about the epitaxial growth of single phase ζ-Fe_2N.

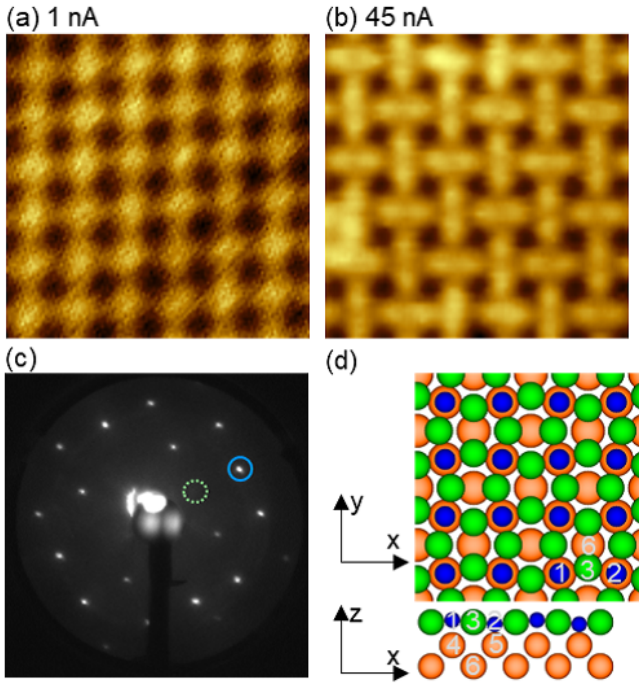

Figure 2.11: (a), (b) Topographic STM image of the Fe_2N monolayer on the Cu(001) substrate scanned at (a) tunneling current $I_t = 1$ nA and (b) $I_t = 45$ nA . (c) LEED pattern of the Fe_2N monolayer on the Cu(001) substrate with the incidence energy of 100 eV. Blue circle indicates the fundamental spot of Cu(001). Those data are measured by ourselves. (d) Schematic model of the Fe_2N monolayer on the Cu(001) substrate. The Fe, N and Cu atoms are described as the green, blue and orange balls respectively. The numbers correspond to the atoms in Table2.1.

Table 2.1: The coordination of the Fe_2N monolayer on the Cu(001) substrate determined by LEED-IV [62]. The number in the first column corresponds to the atoms in Fig. 2.11 (d).

No.	x (Å)	y (Å)	z (Å)
1	0	0	0.23
2	3.62	0	-0.24
3	1.81	0.39	0.04
4	0	0	-1.85
5	3.62	0	-1.83
6	1.81	-1.81	-1.86
7	1.84	0	-3.57

2.8 Iron nitride monatomic layer on the Cu(001) substrate

The Fe_2N monatomic layer is fabricated on the Cu(001) substrate by the N^+ ion bombardment on the clean Cu(001) substrate, 2 monolayer (ML) Fe deposition in ultrahigh vacuum (UHV) at room temperature (RT) and subsequently annealing at 580 K [15,62]. Figures 2.11 (a), (b) and (c) show the topographic STM images and LEED pattern of the Fe_2N monolayer on the Cu(001) substrate. The detail of the structure with a $p4gm(2\times2)$ lattice is determined by the LEED-IV measurements as shown in Fig. 2.11 (d) and Table 2.1 [62]. The two Fe atoms close to each other are seen as protrusions at tunneling current $I_t = 45$ nA in the topographic STM images.

As shown in Fig. 2.11 (b), the topographic STM image of the Fe_2N monolayer depends on the tunneling current. At the large tunneling current, the dumbbell shapes are observed by STM. Two humps in the dumbbell shapes are located at the position of the Fe atoms. In contrast, at the small tunneling current, the dots are observed at the center position of the dumbbell shapes which correspond to the N-absent sites. This change in the topographic STM image is described by the dependence of the tunneling probabilities on the tip sample distance [14]. At the long tip sample distance, the STM tip sensitively proves the outer orbital of the surface. As closing the tip-sample distance, the STM tip can sensitively prove other inner orbitals of the surface. Therefore, at the short tip-sample distance, the Fe atoms are observed as protrusions since the inner d orbital of the Fe_2N monolayer is relatively sensitively proven. In contrast, at the long tip sample distance, the s/p orbitals are observed. The N atoms are located at the depressions in the topographic STM images.

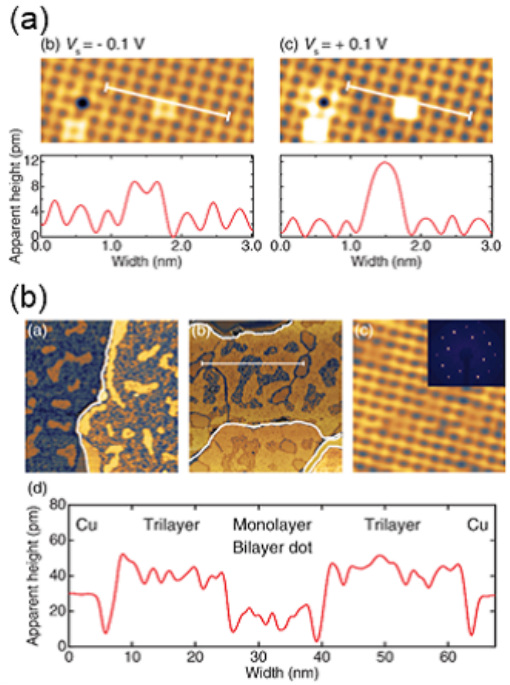

Figure 2.12: (a) Bright protrusions at the N sites of the Fe_2N monolayer. (b) Topographic STM image of the γ'-Fe_4N trilayer. (a) taken from Fig. 2 in [15]. (b): taken from Fig. 4 in [15]

The XAS/XMCD measurement indicates that the Fe_2N monolayer on the Cu(001) substrate exhibits ferromagnetism with an in-plane magnetic anisotropy at 8 K. The spin magnetic moment of the Fe_2N monolayer at 8 K is estimated to be 0.8 μ_B/atom [62] and 1.1 μ_B/atom [15] by XMCD sum rule. We assume that the difference in the magnetic moment is due to the quality of the sample.

At the low annealing temperature, some defects are observed at the Fe position. As increasing the annealing temperature, the number of defects at the Fe sites becomes low, and instead some bright protrusions are observed as shown in Fig. 2.12 (a). The number of these bright protrusions increases with increasing the annealing temperature. While the apparent height of the bright dots is 10 pm at the positive bias voltage, that at the negative bias voltage is 5 pm. They are observed since the Cu atoms under the N atoms are substituted by Fe atoms during the annealing process [15]. Here, we refer to these bright dots as bilayer dots.

Y. Takagi *et al.*, [62] claimed that the 1-4 ML iron nitride layers are fabricated by repeating the cycle of the N^+ ion bombardment, Fe deposition and subsequent annealing. The thickness was estimated by the Fe $L_{2,3}$ and N K edge and all LEED pattern of 1-4 ML iron nitride layers were $p4gm$ pattern. In

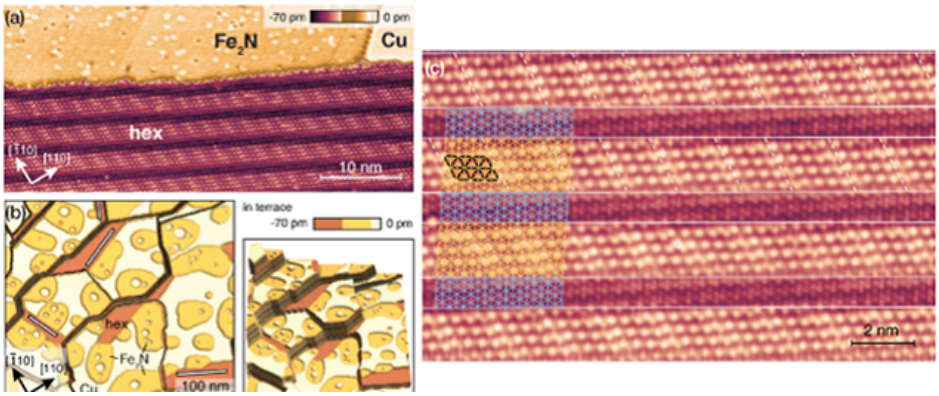

Figure 2.13: Hexagonal iron nitride monolayer on the Cu(001) substrate : taken Fig. 1 in [16]

other group, Y. Takahashi *et al.*, [15] fabricated iron nitride layer by the same procedure. However, they observed only Fe_2N monolayer with at most 40% bilayer dots by using STM while repeating the cycle four times. Therefore, the amount of the Fe was at most 2 ML which is in conflict with the results by Y. Takagi *et al.*,.

Y. Takahashi *et al.*, uses the other way to fabricate the γ'-Fe_4N trilayer as following step; First, they grew the Fe_2N monolayer on the Cu(001) substrate. Then, 2 ML Fe was deposited under the N_2 atmosphere while the sample was kept at RT. Finally, the sample was annealed at 600 K. They observed γ'-Fe_4N trilayer regions as shown in Fig. 2.12 (b). In addition, the thickness estimated from the XA spectra was 3 ML. Since the sample fabricated by Y. Takagi *et al.*, only mention the surface structure by the $p4gm(2\times2)$ LEED pattern, it is possible that some Fe cluster or other disorder regions can remain at the subsurface. We consider that only the fabrication procedure conducted by Y. Takahashi *et al.*, can obtain the γ'-Fe_4N trilayer.

The magnetic moment of the sample containing the γ'-Fe_4N trilayer regions is 1.4 μ_B/atom which is larger than that of the Fe_2N monolayer of 1.1 μ_B/atom [15]. The film also has an in-plane magnetic anisotropy. According to the first principle calculation [15], magnetic moment of the Fe_2N top layer of the Fe_4N trilayer is 1.8 μ_B/ atom. However. that of the Fe atoms of the Fe_4N trilayer bonding with Cu of the Cu(001) substrates is 0.62 μ_B/atom.

By supplying the excess N atoms, the other hexagonal iron nitride film grows near the step edge of the Cu(001) substrate [16]. The nearest distance between the protrusions is 310±10 pm which is very similar to the Fe-Fe distance in a (111) plane of $\gamma''-$FeN. Therefore, K. Ienaga *et al.*, [16] claimed that the FeN film is fabricated. The symmetry difference between the film and

substrate makes a stripe superstructure as shown in Fig. 2.13.

Chapter 3

Measurement systems

3.1 Experimental system overview

3.1.1 STM measurements

The STM measurements were conducted in an UHV chamber, which consists of two chambers, a preparation chamber and an STM chamber as shown in Fig. 3.1 (a). The preparation chamber is equipped with an ion gun, an annealing base, Fe and Co EFM evaporates (FOCUS), and a LEED system. All sample preparation process for the STM observation were conducted in this preparation chamber with the base pressure of better than 1.0×10^{-10} Torr. The chamber is evacuated by tandem molecular turbo pumps and a rotary pump. The titanium sublimation pump is used to achieve better vacuum. The sample can be transferred to the STM chamber from the preparation chamber under 1.0×10^{-10} Torr without breaking the vacuum. The base pressure of the STM chamber was better than 3.0×10^{-10} Torr by using an ion pump. The sample is cooled at 80 K by using liquid N_2. Topographic STM images are taken with a constant current mode by operating the Nanonis SPM control system. The chemically-edged W is used as a tip [63]. The STM data are analyzed by using a software for data analysis; WsXM [64] and Gwyddion [65]. The differential conductance dI/dV spectra is obtained by a conventional lock-in amplifier with a bias modulation of 20 mV and with a modulation of frequency at 717 Hz.

3.1.2 XPS measurements

Figure 3.1 (b) shows a chamber used for the XPS measurement. It also consists of two chambers, a preparation chamber and an XPS-measurement chamber. In the preparation chamber with the base pressure of below 2.0×10^{-11} Torr, there are an ion gun, a sample annealing system by direct current heating,

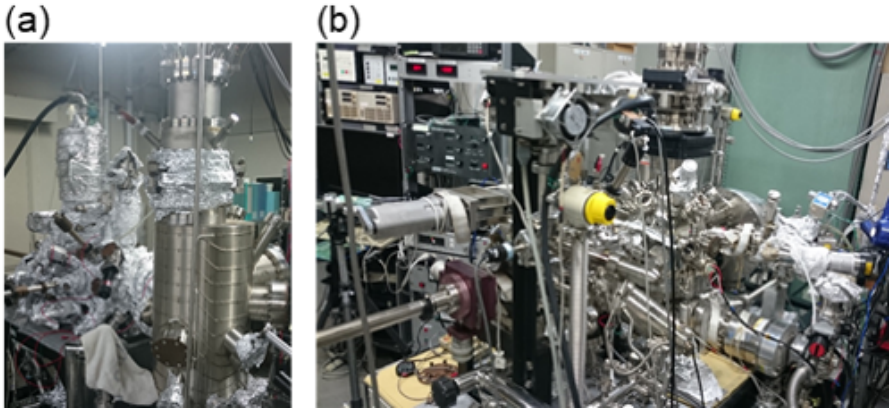

Figure 3.1: UHV chambers for (a) STM and (b) XPS

a thickness monitor and two evaporators. The samples were prepared in the preparation chamber. In the XPS-measurement chamber which is connected to the preparation chamber, there are a LEED system, a hemispherical analyzer (SES100, Scienta) and a twin Mg K_α and Al K_α anode X-ray source. The X-ray is irradiated to the sample at the 60-degree rotated direction from the sample normal direction.

3.1.3 XAS/XMCD measurements

The XAS and XMCD measurements were conducted at Ultra Violet Synchrotron Orbital Radiation (UVSOR) Ⅲ BL-4B, the facility of the Institute for Molecular Science (IMS), Okazaki, Japan [66, 67]. A variedline-spacing plane grating monochromator (VLS-PGM) based on the Hetrrick-type design [66] is used to achieve high energy resolution as shown in Fig. 3.2. The magnetic field can be applied up to $B = \pm 5$ T in the direction parallel to the X-ray incidence. It is generated by using superconducting magnet which is cooled by liquid He. The XAS/XMCD measurements were conducted at 8 K by total electron yield (TEY) mode. The circular polarization was 50 - 65 % which was checked by the saturation magnetization of the thick Fe film every beamtime. The angle θ defined as the angle between the sample normal direction and the X-ray incidence can be freely changed by rotating the sample manipulator. We usually measure the XA spectra at $\theta = 0°$ as well as at $\theta = 55°$. The samples were fabricated at the other UHV chamber in which the sample can be transferred from the measurement chamber. The base pressure was better than 5.0×10^{-10} Torr. The chamber is evacuated by a tandem molecular turbo pump and a rotary pump. In addition, a titanium sublimation pump and a NEG pump are used. An ion gun, an annealing base with a thermocouple, evaporators, a thickness monitor, a mass monitor, LEED system are equipped

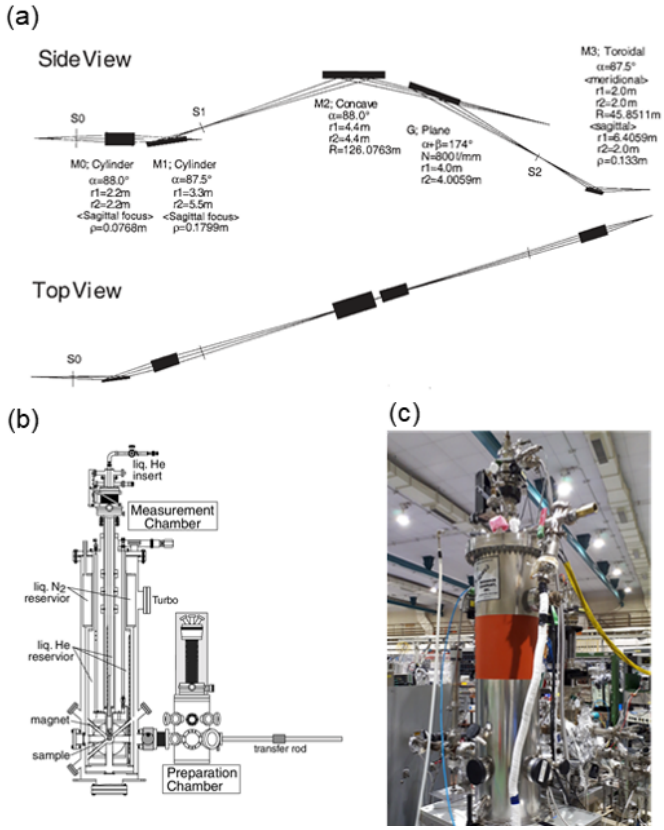

Figure 3.2: (a) Layout of the VLS-PGM beamline BL 4B at UVSOR Ⅲ (b) Schematic view of the XAS/XMCD measurements chamber. (c) Image of the XAS/XMCD measurements chamber. (a): taken from Fig. 1 in [66] (b): taken from Fig. 1 in [67]

in the preparation chamber.

3.2 Sample preparation

First, we show the detail of the sample preparation in STM chamber. Then, we show the difference between the procedures in STM chamber and those in other chambers.

3.2.1 Cleaning Cu substrates

We used single crystals Cu(111) (ϕ = 6 mm and 5 mm) and Cu(001) (ϕ = 4 mm) in our STM and XPS measurement. First, the sample was cleaned by the chemical etching by using nitric acid and methanol under 230 K. Then, the crystal was mounted on a molybdenum sample holder by fixing a tantalum wire. After the sample was transferred to the chamber, the sample was cleaned

by the following step. First, Ar^+ sputtering was conducted by the ion gun under the pressure of Ar gas of 2.0×10^{-5} Torr with the ion energy of 1 keV. Then, the sample was annealed at 900 K by electron bombardment emitted from the W filament. The temperature during the annealing process was monitored by a pyrometer. The surface cleanness was checked by STM and the sharp shots of LEED.

3.2.2 N^+ ion bombardment

N atoms were bombard by the ion gun with the ion energy of 500 eV under the pressure of N_2 gas of 1.0×10^{-5} Torr for 15 min. After we performed the N^+ ion bombardment on the Cu substrate at this condition and subsequently annealing at 530 K, we confirmed the N-saturated Cu(001) surface [68] and Cu(111) surface [69]. Therefore, the N atoms can adsorb sufficiently on the Cu substrates by this condition.

3.2.3 Fe and Co deposition

Iron and cobalt were deposited from high purity Fe (99.998 %) and Co rod (99.998 %) by using EFM evaporators (FOCUS). In order to avoid contamination, the pressure in the chamber must be better than 1.5×10^{-10} Torr. During the deposition, the sample was kept at RT. The deposition rate was estimated by depositing each material on the Cu substrate under the UHV condition and measuring the coverage of Fe and Co islands on the Cu substrates in the topographic STM images. The deposition rate of Fe and Co were 0.3 monolayer (ML)/min and 0.1 ML/min respectively. Here, 1 ML is defined as the Cu atomic density on the Cu substrates. The topographic STM images of Fe islands on the Cu(111) substrate and Co islands on the Cu(001) substrate are shown in Figs. 3.3 (a) and (b). It should be noted that the bilayer Fe islands are grown on the Cu(111) substrate [70].

3.2.4 Difference in the sample preparation condition

In principle, the sample preparation condition in the STM chamber is the same as that in the XPS chamber. The only difference is the heating system. While the samples were annealed by an electron bombardment in the STM chamber, those were annealed by an electrical heating in the XPS chambers. The annealing temperature was measured by a pyrometer both in the chamber.

Next, we show the difference in the sample preparation system between the STM chamber and the XAS chamber. In the Ar^+ sputtering and N^+ ion bombardment, the pressure of N_2 gas and Ar gas were about 4.0×10^{-7} Torr at the XAS chamber. After the N^+ ion bombardment with the ion energy of

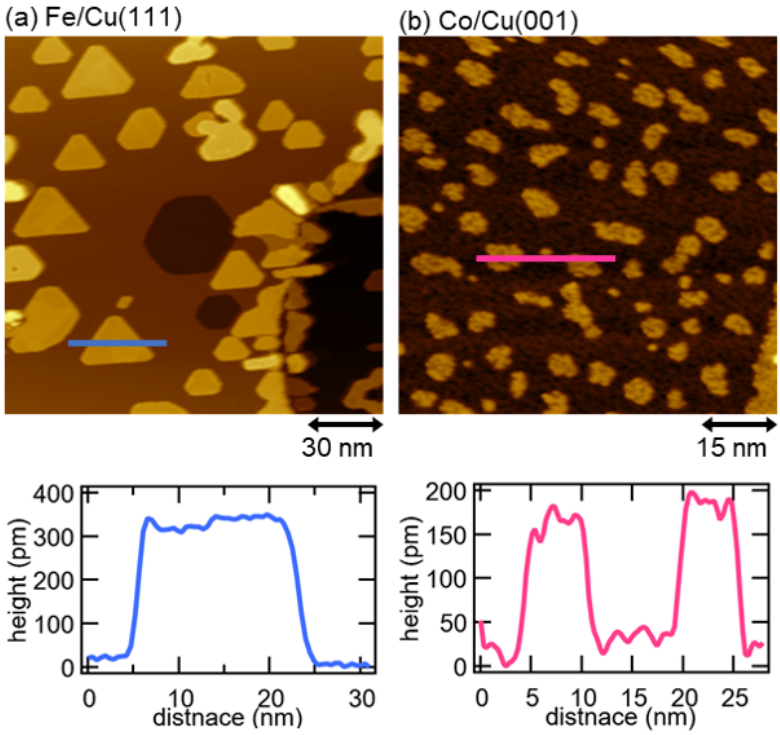

Figure 3.3: (a), (b) Topographic STM images of (a) Fe islands on the Cu(111) substrate and (b) Co islands on the Cu(001) substrate. The height profiles along the lines in the STM images are shown at the bottom.

200 eV under the N_2 gas atmosphere with the pressure of 4.0×10^{-7} Torr for 15 min and subsequently annealing at 530 K, the N-saturated Cu(001) surface was observed by using LEED [71]. Therefore, we used this condition for the N^+ ion bombardment. The annealing temperature at the XAS chamber was monitored by a C-type thermocouple. For the Fe and Co deposition, we also used EFM evaporators. At the XAS measurement, the thickness monitor was used to estimate the Fe and Co deposition rate.

The LEED pattern are used to confirm that the same samples were fabricated in each chamber.

Chapter 4

Lattice distortion of square iron nitride monolayers induced by changing symmetry of Cu substrates

4.1 Introduction

The lattice of the magnetic monolayer films grown epitaxially on the substrate can be distorted by the lattice mismatch between the substrate and the film [72–74]. This enables us to tune their electronic and magnetic properties such as the band gap [73, 74], easy magnetization axis [75, 76], magnetic moment [49,77] and so on. As for the iron nitride film, it is reported that the saturation magnetization of the γ'-Fe_4N film is tuned by changing the substrates from $LaAlO_3$(001) to MgO(001) [49].

Although the epitaxial growth is the major way to grow the magnetic films on the substrates, the appropriate substrates should be selected from the limited substrates. The lattice constant and the coefficient of the thermal expansion of the substrates must be similar to those of the films [78]. Recently, some single or a-few-monolayer films with a robust in-plane bonding, such as transition metal dichalcogenides, hexagonal boron nitrides, and metal carbides [79, 80], have drawn much attention. They can retain their structure irrespective of the substrates by taking advantage of the high stability of the films [80]. As for the magnetic film, few-atomic-layer films of van der Waals materials grown by chemical vapor transport are explored [81–83]. Moreover, some ferromagnetic monolayer alloys with robust in-plane bonds such as $GdAg_2$ [84], $GdAu_2$ [85] and Fe_2N [62] have been reported.

In order to fabricate the new iron nitride monolayers, we focus on the

stability of the transition metal nitride monolayer films with a square lattice since they are stabilized by the robust covalent bond of N atoms with the metal atoms. It is reported that monolayer films with rectangular or square lattices can grow on the fcc(111) substrates with hexagonal lattices in several systems such as N/Cu(111) [69, 86], C/Ni(111) [87, 88], and S/Ni(111) [89], which has been considered as adsorption-induced reconstruction by N, C and S. Increasing the number of the robust covalent bonds from 3 to 4 overcomes instability induced by the difference in symmetry between the substrates and the films [88]. By the robust covalent bonds between Fe and N atoms [9], we expect that the square iron nitride films are fabricated on the Cu(111) substrate as observed in the square Cu_2N monolayer on the Cu(111) substrate [69].

In this chapter, we describe the growth and structure of iron nitride films on the Cu(111) substrate by a similar way to fabricate the square Fe_2N monolayer on the Cu(001) substrate [15]. In order to determine the structure, we have combined an atomic-scale observation by STM with spatially-averaged observations by LEED and XPS. We show the proposed structure models of their monolayer films.

4.2 Experimental method

The STM measurement system and the procedure of cleaning the Cu(111) substrate are described in Chapter 3. Iron nitride monolayers were fabricated by N^+ ion bombardment on the clean Cu(111) substrate, Fe deposition in UHV at RT and subsequent annealing.

The detail in the XPS measurements is shown in Chapter 3. The fabrication procedure for iron nitride monolayers in the XPS chamber was similar to that in the STM chamber and the surface structures were confirmed by LEED. The Mg K_α source was used to measure the Fe2p core level and Al K_α source was used to measure the N1s core level. The spectra were obtained at RT. The Cu2$p_{3/2}$ core level of the Cu crystal at 932.7 eV was used for the calibration of the binding energy measured by each X-ray source [90].

4.3 Results and Discussion

4.3.1 Two ordered iron nitride monolayers

After the 1 ML Fe deposition on the N-bombard Cu(111) substrate followed by annealing at 510 K and 580 K, two ordered structures shown in Figs. 4.1 (a) and (b) were observed by STM. In both structures, the protrusions are almost

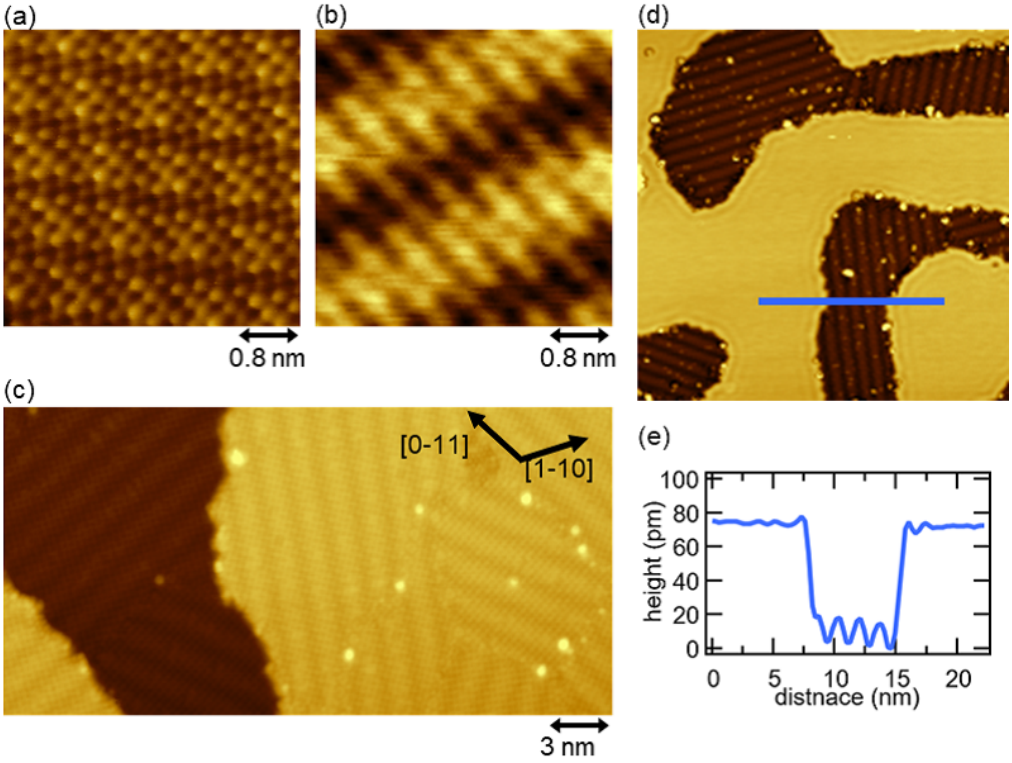

Figure 4.1: (a), (b) Atomically-resolved topographic STM images of iron nitride monolayers after the annealing at (a) 510 K and (b) 580 K. They are scanned at the sample bias voltage $V_b = 500$ mV and tunneling current $I_t = 5.0$ nA, and (b) at $V_b = 50$ mV, and $I_t = 1.0$ nA. (c) Large scale topographic STM image of an iron nitride monolayer film obtained by the annealing at 580 K with $V_b = 2.0$ V and $I_t = 1.0$ nA. (d) Large scale topographic STM image of an iron nitride monolayer film obtained by the 0.4 ML Fe deposition and subsequent annealing at 580 K with $V_b = 0.3$ V and $I_t = 0.5$ nA. (e) Height profile along the blue line in (d).

squarely arranged. The nearest protrusion distance are 268 ± 10 pm in Fig. 4.1 (a), and 355 ± 10 pm in Fig. 4.1 (b). The latter distance is close to the nearest N-N distance of the Fe_2N monolayer on the Cu(001) substrate [15,62].

Figure 4.1 (c) displays the large scale topographic STM image of the surface shown in Fig. 4.1 (b). The stripe superstructure of 1.7 nm periodicity was formed along the ± 18° rotated direction from the close packed direction of the Cu(111) substrate and six equivalent structural domains with different stripe direction were observed. The apparent height difference in the stripe superstructure was 18 pm at the sample bias voltage $V_b = 50$ mV. Here, we refer to the structure shown in Fig. 4.1 (a) as the dotted structure and the

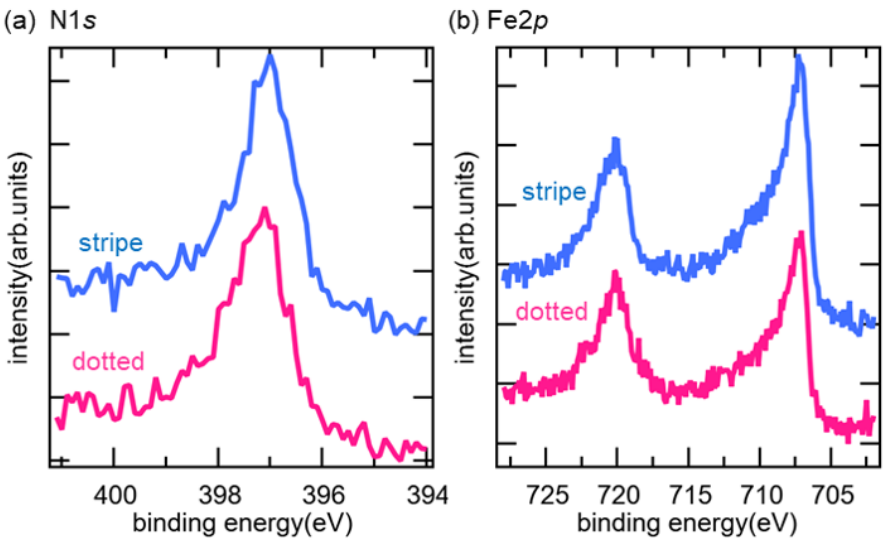

Figure 4.2: (a), (b) XPS of (a) N1s core level and (b) Fe2p core level. Red (blue) line indicates XPS of the iron nitride monolayer film annealed at 510 K (580 K) which corresponds to the dotted (stripe) structure.

structure shown in Figs. 4.1 (b) and (c) as the stripe structure.

After the 0.4 ML Fe was deposited instead of 1 ML, each structure co-existed with the bright regions. The topographic STM image of the stripe superstructure fabricated by 0.4 ML Fe deposition is shown in Fig. 4.1 (d). We confirmed the bright regions are the bare Cu(111) regions by observing the standing wave near the step edge and defects. They were apparently 80 pm higher than the iron nitride regions at $V_b = 0.3$ V as shown in Fig. 4.1 (e). This indicates that the iron nitride layers are located at the same layer as the bare Cu(111) regions. In addition, this suggests that each films are monatomic layer films.

4.3.2 XPS study

The XPS measurements for N1s and Fe2p core level were conducted to estimate the chemical composition of iron nitride monolayer on the Cu(111) substrates. Figures 4.2 (a) and (b) display the XPS of N1s and Fe2p core level of each structure. The N1s peak of the dotted and stripe structure were located at 397.2 eV and 397.1 eV, respectively. They are lower than the N1s core level of the Fe_2N top layer of 1.5 nm thick γ'-Fe_4N film [61] which has a peak at 397.8 eV. In addition, they are higher than that of the N-adsorbed Cu(001) substrate which is located at 396.2 eV [91].

The Fe2$p_{3/2}$ peaks of dotted and stripe structures appeared at 707.4 eV

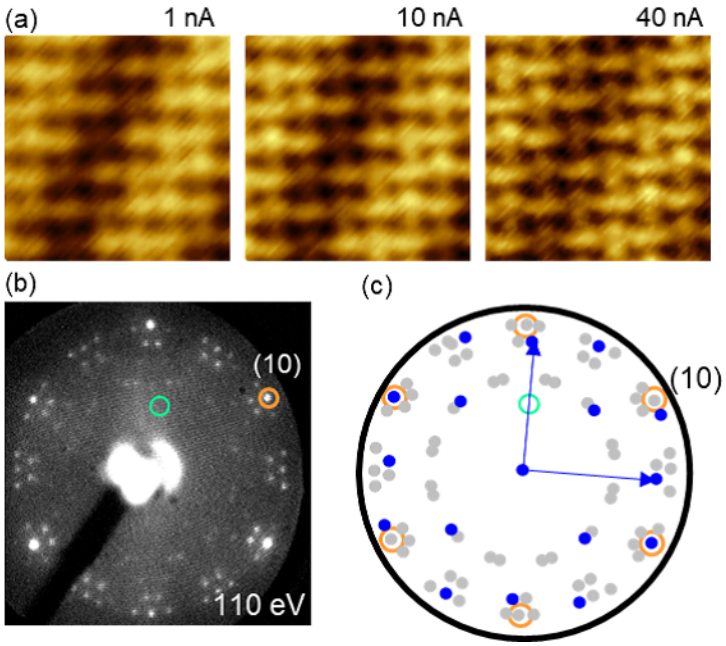

Figure 4.3: (a) Tunneling current dependence on topographic STM images of the stripe structure at V_b= 50 mV and I_t = 1.0, 10, and 40 nA. (b) LEED pattern of the stripe structure at the incidence energy of 110 eV. (c) Schematic LEED pattern of the stripe structure corresponding to (b). Blue circles indicate the LEED pattern from the single domain. The blue arrows show the reciprocal primitive vectors of the stripe structure. Orange circles in (b) and (c) show the fundamental spots of the Cu(111) substrate.

which were very similar to those observed in the 1.5 nm thick γ'-Fe_4N [61] and other iron nitride thin films [92,93]. However, the peak energy was higher than that of Fe crystal at 706.7 eV. This is attributed to the charge transfer from Fe to N. The weak satellite peaks appeared at 713-715 eV are ascribed to the shake-up satellite peak [94,95].

The Fe2$p_{3/2}$ peak positions is strongly related to the ionic valence of Fe. According to the previous researches [96,97], the Fe2$p_{3/2}$ peak of Fe^0, Fe^{2+} and Fe^{3+} are located at about 707 eV, 708-709 eV and 710-711 eV, respectively. The Fe2$p_{3/2}$ peaks of dotted and stripe structures at 707.4 eV are associated with Fe^0 as seen in the γ'-Fe_4N films [61,98].

In order to investigate the chemical composition, the peak area of Fe2$p_{3/2}$ and N1s were calculated after subtracting the background by the Shirley method [22]. Considering the relative sensitive factor and ionization cross section [99], the chemical composition of the dotted and stripe structures are estimated to be $Fe_{1.8\pm0.2}N$ and $Fe_{2.2\pm0.2}N$, respectively.

4.3.3 Clock reconstruction of the stripe structure

The topographic STM image of the stripe superstructure is strongly dependent on the tunneling current I_t as shown in Fig. 4.3 (a). As increasing the tunneling current, protrusions seen as dots at $I_t = 1.0$ nA gradually changed toward an ellipse shape elongated along the two perpendicular direction. Finally, at $I_t \geqq 30$ nA, the dumbbell shape with two humps were observed. As described in Chapter 2, a similar dependence of the topographic STM image on the tunneling current is observed on the Fe_2N monolayer on the Cu(001) substrate since the tunneling probabilities of outer s/p orbital on the tunneling current is different from those of inner d orbitals.

In addition to similar dependence of topographic STM image on the tunneling current to the Fe_2N monolayer on the Cu(001) substrate, the chemical composition of the stripe structure of $Fe_{2.2\pm0.2}N$ estimated by XPS indicates that the square Fe_2N monolayer with a clock reconstruction is fabricated on the Cu (111) substrate. It should be noted that the N atoms are located at the depression sites in the topographic STM image.

The LEED pattern of the structure shown in Fig. 4.3 (b) also indicates the clock reconstruction of the Fe_2N monolayer with the plane symmetry group of $p4gm$. Considering that the nearest distance between the protrusions in the STM images and the crystal orientation of the Cu(111) substrate, the spots corresponding to the (1/2, 0) spot of the Fe_2N monolayer on the Cu(001) substrate should be located at the green circles in Figs. 4.3 (b) and (c). The absence of the (1/2, 0) spots at a wide incident energy of 40 to 200 eV demonstrates that the clock reconstruction occurs even at the Fe_2N monolayer on the Cu(111) substrates.

It is known that the surface Fe_2N layer on the γ'-Fe_4N film exhibits the clock reconstruction [10,100]. According to the first principles calculation, the clock reconstruction stabilizes the Fe_2N layer compared with unreconstructed layer at the nearest N-N distance of 365 pm or 382 pm [100]. This is explained by the stabilization of the surface iron nitride layer by the expansion of the nearest Fe -N distance. This would also stabilize the Fe_2N monolayer even on the Cu(111) substrate.

By the STM measurements, it is reported that the C-adsorbed Ni(111) substrate also forms the square lattice and induces the clock reconstruction [88]. The LEED pattern of the C-adsorbed Ni(111) substrate [87] is similar to Fig. 4.3 (b).

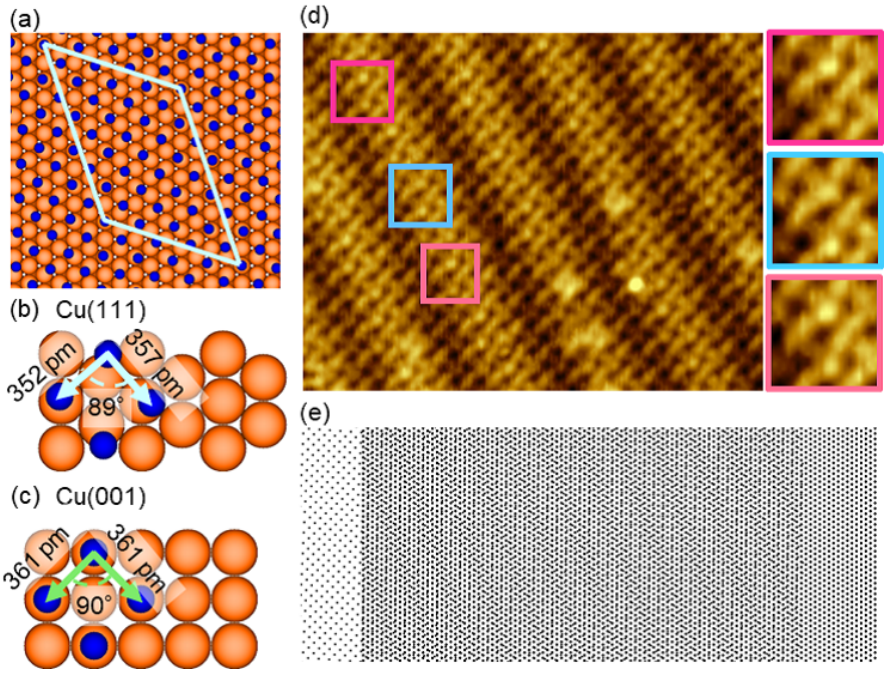

Figure 4.4: (a) Schematic model of the stripe structure. Orange and blue balls show Cu and N atoms, respectively. Unit cell of the Fe_2N monolayer films (b) on the Cu(111) substrate and (c) Cu(001) substrate. (d) Topographic STM image at V_b= 50 mV and I_t = 40 nA. The red, blue and pink squares in the right images show the magnified images of the left image indicated by the red, blue and pink squares, respectively. (e) The moiré pattern between the hexagonal Cu(111) lattice and Fe_2N monolayer lattice. The model in (b) was used as the lattice constant of the Fe_2N monolayer.

4.3.4 Stacking of the Fe_2N monolayer on Cu(111) substrate

The two blue arrows in Fig. 4.3 (c) corresponding to the reciprocal primitive vectors was slightly larger than 90°. In addition, the nearest neighbor N-N distance estimated by LEED pattern was slightly shorter than that of the square Fe_2N monolayer on the Cu(001) substrate of 361 pm. This suggests that the lattice of the Fe_2N monolayer on the Cu(111) substrate is distorted toward a monoclinic lattice. It should be noted that the lattice constants of all six domains of the stripe structure from the same LEED pattern were the same. Therefore, the distortion is not attributed to the experimental misalignment between the sample position and LEED, but to the intrinsic lattice distortion induced by the difference of symmetry between the Cu(111) substrate and the Fe_2N monolayer.

From these STM and LEED results of the lattice constant and lattice orientation of the stripe structure, a model of the Fe_2N monolayer on the Cu(111) substrate is proposed as shown in Fig. 4.4 (a). The unit cell with the consideration of the Cu substrate indicated by the light blue arrows in Fig. 4.4 (a) is denoted as $\begin{pmatrix} 9 & -2 \\ 4 & 8 \end{pmatrix}$ by the conventional matrix notation [101]. In this model, the lattice is distorted toward a monoclinic lattice compared to a square Fe_2N monolayer on the Cu(001) substrate. The detail of the lattice constant are shown in Figs. 4.4 (b) and (c). This schematic model reproduce the direction and the periodicity of the stripe moiré pattern observed in the STM well as shown in Fig. 4.4 (e) which is also the evidence that our schematic model reflects the actual structure. Note that the moiré pattern could not be reproduced by using a square or rectangular lattice of the iron nitride monolayer.

Although the dumbbell shapes in the topographic STM image of the Fe_2N monolayer obtained at a short tip-sample distance are homogeneous, those on the Cu(111) substrate shown in Fig. 4.3 (a) and Fig. 4.4 (d) are asymmetric. The apparent height difference between the two humps of the dumbbell shape was 0 - 4 pm. The asymmetric shape was changed periodically. As seen in the red and pink box in Fig. 4.4 (e) which are the same position in each unit cells, the periodicity is the same one as the unit cell of our model. Therefore, the change in the apparent height was owing to the stacking geometry of Fe on the Cu(111) substrates.

4.3.5 Structural modulation of the stripe structure

Bias dependence of the height profile of the stripe superstructure along the blue dotted line on the topographic STM image in Fig. 4.5 (c) are shown in Figs. 4.5 (a) and (b). The height of the stripe superstructure is constantly 18 pm at V_b = 0.5 - 2.0 V while that at V_b = 3.0 V is to 13 pm. Bias independence on the apparent height at the low bias voltage indicates that the stripe superstructure is attributed to an actual geometrical corrugation. On the basis of the schematic model in Fig. 4.4 (a), the horizontal distance from each N atoms to the closest subsurface Cu atoms are calculated. The color of the balls in Fig. 4.5 (d) correspond to the horizontal distance. The N atoms indicated by white balls are located at the atop sites of the Cu atoms since the horizontal distance from N atoms to the nearest Cu atoms is almost zero. In contrast, the dark blue balls describe the N atoms at the hollow sites of the Cu atoms. We can recognize that a period of the stripe pattern of the color in Fig. 4.5(d) is consistent with the stripe superstructure with the STM images shown in Fig. 4.5 (c). This result indicates that the observed geometrical

corrugation is attributed from the stacking difference in the N atoms on the Cu (111) substrates.

When the Fe_2N monolayer was prepared by higher annealing temperature, some protrusions apparently higher than those of Fe atoms are observed at the N sites as indicated by purple balls in Fig. 4.6 (a). They were 10 - 25 pm higher than the protrusions of Fe at $V_b = 50$ mV and the apparent height depended on the tunneling current and the sample bias voltage. As explained in Chapter 2, similar protrusions are observed on the Fe_2N monolayer on the Cu(001) substrate when some Cu atoms at the subsurface are substituted to Fe atoms and local density of states are increased by the hybridization between Fe and N atoms. Similarly, in the case of the Cu(111) substrates, we consider that these apparently-higher protrusions are observed by the subsurface Fe atoms. Here, we refer to these apparently-higher protrusions as bilayer dots. The bilayer dots are mainly located at the bright regions in the stripe superstructure as shown in Fig. 4.6 (a). By using our schematic model, we can describe that the bilayer dots are selectively located near the atop sites of the substituted Cu atoms as indicated by purple and red balls in Fig. 4.6 (b). This result is consistent with our assumption that most of the N atoms at the bright regions are located at the atom sites of the Cu atoms as described in Fig. 4.5 (d).

Here, we discuss the stability of the monolayers with the rectangular and square lattices on fcc(111) substrate. As mentioned above, increase in the covalent bond between the adsorbate and surface metal atoms from 3 to 4 stabilize the square lattice on the fcc substrates [88,102–104]. Moreover, some atoms on the fcc(111) substrate are stabilized by the covalent bond with the second layer atoms in addition to the four in-plane bonds by being located on atop sites of the fcc(111) substrate [88, 103]. As for the nitride layers, a density functional calculation for the Cu_2N monolayer on the Cu(111) substrate reveals that the total binding energy of a square Cu_2N monolayer on the hexagonal Cu(111) substrate is larger than that for the hexagonal copper nitride monolayer on the Cu(111) substrate [103]. Therefore, we assume that the robust covalent bond of N with Fe atoms stabilizes the square Fe_2N monolayer on the hexagonal Cu(111) substrates. Furthermore, we consider that the Fe_2N monolayer on the Cu(111) substrate is stabilized by the modulation of Fe atoms at the normal direction to the surface. The modulations of the apparent height of the square or rectangle lattice on the fcc(111) substrate was also reported in several systems such as Cu_xS on Au(111) [104], and NiO on Pt(111) [105].

4.3.6 Schematic model of the dotted structure

In this subsection, we propose a schematic model of the dotted structure. As the Fe atoms of the square Fe_2N monolayer are seen as protrusions at a

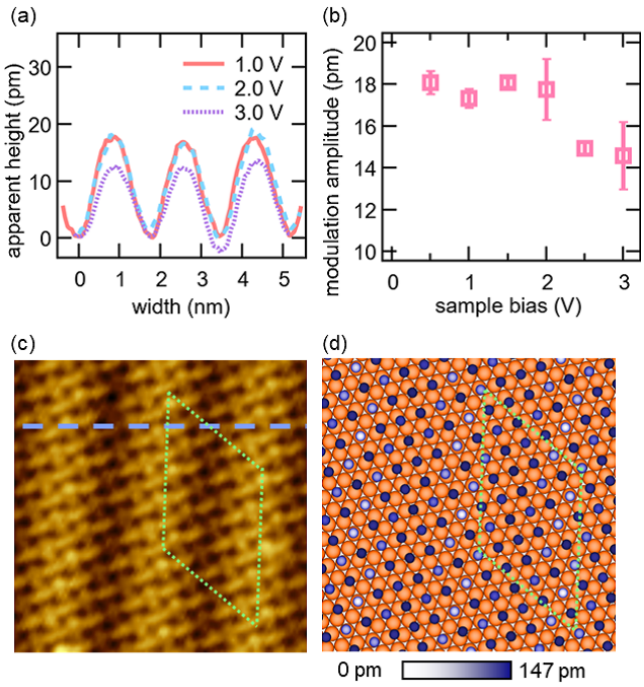

Figure 4.5: (a) Apparent height along the blue dotted line in the topographic STM image of (c) at V_B = 1.0, 2.0, and 3.0 V. (b) Bias dependence on the apparent height modulation amplitude of the stripe superstructure at positive bias voltage. (c) Topographic STM image of the Fe_2N monolayer on the Cu(111) substrate obtained at V_B = 50 mV and I_t = 40 nA. (d) Schematic model of the Fe_2N monolayer on the Cu(111) substrate. The size is the same as the topographic STM image of (c). Cu atoms are indicated by orange balls. The N atoms are indicated by other balls. The color of balls display the horizontal distance from the nearest Cu atoms. Green parallelograms in (c) and (d) show the unit cell with respect to the Cu(111) substrate.

short tip-sample distance, we simply assume that the Fe atoms are observed as protrusions by STM. Although the topographic STM image of the dotted structure is measured by changing a tunneling current, topographic STM image was independent on the tunneling current.

By the XPS measurement, the chemical composition of the dotted structure was estimated to be $Fe_{1.8\pm0.2}N$. The nearest distance between Fe atoms are 248 pm in bulk Fe and 268 pm in γ'-Fe_4N [10]. However, if the N atoms were observed as protrusions, the nearest distance between Fe atoms would be less than 200 pm and the density of the surface atoms would be much higher. Therefore, from the surface Fe density, it is excluded that the N atoms are seen as protrusions.

Figures 4.7 (a) and (b) display large scale topographic images of the dotted

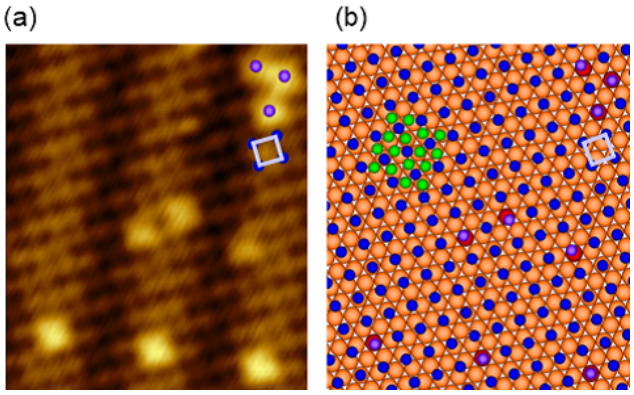

Figure 4.6: (a) Topographic STM image recoded at $V_B = 50$ mV and $I_t = 1.0$ nA. Blue balls indicate the N atoms which are imaged as depressions. Purple balls indicate the positions of the N atoms on apparently-high protrusions at the top-right area. (b) Schematic model of Fe_2N/Cu(111) corresponding to the topographic STM image of (a). Blue and purple balls show N atoms, green and red Fe atoms, and orange Cu atoms. The red Fe atoms are in the substrate Cu lattice. Three purple balls at the top-right area are located on the same positions as those in (a).

structure. The six equivalent domains with different orientation were observed. Protrusions in Fig. 4.7 (b) are aligned with 1.0 nm periodicity. While no difference of these protrusions were recognized with a blunt tip, three patterns as indicated by red, pink and purple circles in Fig. 4.7 (c) are aligned in order. This change in the pattern is attributed to the stacking difference of the Cu(111) substrate. Therefore, the unit cell size of the dotted structure can be drawn as white dotted parallelograms shown in Fig. 4.7 (c). Considering the crystal orientation and the length of the periodicity, the unit cell with the consideration of the Cu(111) substrate is denoted as $\begin{pmatrix} 3 & 5 \\ -5 & 8 \end{pmatrix}$ in the conventional matrix notation [101]. The 8 protrusions indicated by green balls in Fig. 4.7 (d) form the minimum atomic unit of the dotted structure. These units are periodically aligned. This unit consists of six protrusions which form a 2×3 rectangle and the other two protrusions which are aligned at a different direction from the rectangle. Here, we call this unit as the minimum cell. There are 5 minimum cells in the unit cell of $\begin{pmatrix} 3 & 5 \\ -5 & 8 \end{pmatrix}$.

The chemical composition of the dotted structure is estimated to be $Fe_{1.8\pm0.2}N$. While the actual stoichiometry of the stripe structure is Fe_2N, the chemical composition of the XPS measurement is $Fe_{2.2\pm0.2}N$. In our XPS measurement, the amount of Fe in the actual film seems to be smaller than that obtained by the XPS measurement. Therefore, we speculate that the chemical composition

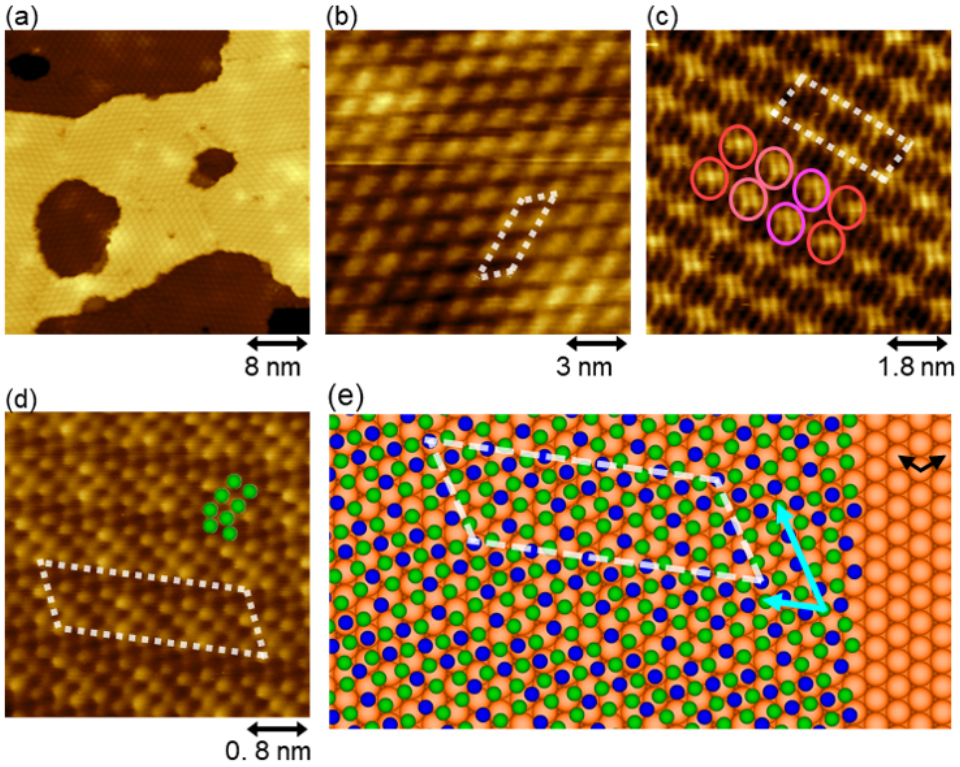

Figure 4.7: (a) Large scale topographic STM image of the dotted structure measured at V_B= 2.0 V, I_t = 1.0 nA. (b) A magnified image of (a). (c) Topographic STM image of the dotted structure measured at V_B= 50 mV and I_t = 5.0 nA. The red, pink, and purple circles indicate different patterns of the apparently higher areas. (d) Atomically-resolved topographic STM image identical with Fig. 4.1 (a). Fe atoms which form the minimum cell are indicated by green circles. (e) Proposed schematic model of the dotted structure. Cu, Fe and N atoms are indicated by orange, green and blue balls, respectively. Black arrows show the primitive vectors of the Cu(111) substrate. The white dotted lines in (b), (c), (d) and (e) show the unit cell. The light blue arrows in (e) indicate the primitive vectors of dotted structure.

of the dotted structure is Fe_8N_5. From our XPS and STM results, we can propose a structure model of the dotted structure as shown in Fig. 4.7 (e). We can speculate the N atoms are located at the fourfold hollow sites of the Fe atoms as observed in N-adsorbed Cu(111) substrate [69,86] or the Fe_2N monolayer on the Cu(001) substrate [15, 62]. However, the actual position cannot be determined from our measurements.

The LEED pattern of the dotted structure at the incidence energy of 50 eV is shown in Fig. 4.8 (a). This pattern is reproduced well by the Fourier

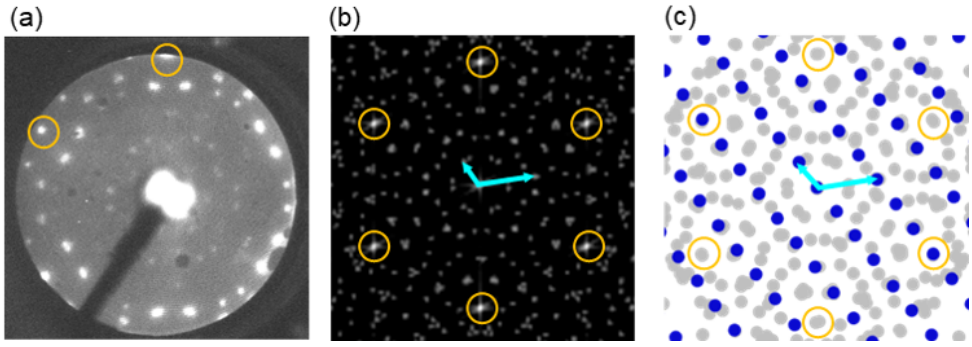

Figure 4.8: (a) LEED pattern of the dotted structure at the incidence energy of 50 eV. The orange circles in (a), (b) and (c) show the fundamental spots of Cu(111). (b) Fourier transform image of the schematic model of Fe and Cu atoms in Fig. 4.7 (e). (c) Schematic LEED pattern of the dotted structure with six domains. Blue circles show the diffraction pattern of a single domain. The light blue arrows in (b) and (c) indicate the reciprocal vectors corresponding to the primitive vectors in Fig. 4.7 (e).

transform image of our schematic model in Fig. 4.7 (e) as shown in Fig. 4.8 (b), which justifies that the unit cell of the dotted structure is denoted as $\begin{pmatrix} 3 & 5 \\ -5 & 8 \end{pmatrix}$. In the Fourier transform image in Fig. 4.8 (b), the patterns with six equivalent domains with the different lattice orientation are involved. It should be noted that one fifth spots of simple diffraction pattern of $\begin{pmatrix} 3 & 5 \\ -5 & 8 \end{pmatrix}$ unit cell was observed as the diffraction pattern since the five minimum cell form the unit cell indicated by the white dotted parallelogram in Fig. 4.7 (d).

Some surfaces such as O/Pd(111) [106] and CH_3S/Cu(111) [107] form the large unit cells on the threefold symmetric substrate. For example, in the O-adsorbed Pd(111) surface, the $Pd_{20}O_{18}$ and $Pd_{32}O_{20}$ structure are more thermodynamically stable than the square and hexagonal film [106] since the complicated structure with large unit cell can reduce the in-plane repulsive interaction. In the case of CH_3S/Cu(111), the adsorbed CH_3S species favor fourfold symmetric sites than threefold symmetric sites [107] because of the in-plane strong inter-molecular interaction. Similarly, in our case, N atoms can stabilize the fourfold symmetric iron nitride monolayer by the robust in-plane bonding between Fe and N.

4.4 Summary

The growth and structure of iron nitride films on the Cu(111) substrate were investigated by using STM, XPS and LEED. An ordered structure was observed after the annealing at 510 K. This ordered structure was changed to another ordered structure with a square lattice after the annealing at 580 K. The XPS measurement revealed that the chemical composition of the dotted structure is $Fe_{2.0\pm0.2}N$ and that of the stripe structure is $Fe_{2.2\pm0.2}N$. In addition, the lattice constant and the unit cell with the consideration of the Cu(111) substrate are estimated from the LEED measurement. By combining with these experimental results, the stripe structure after the annealing at 580 K was the square Fe_2N monolayer with a clock reconstruction. This structure is similar to the structure observed on the Cu(001) substrate. Because of the stacking geometry difference, the lattice is distorted toward a monoclinic lattice. In addition, the actual height is periodically changed along the stripe superstructure due to the stacking difference. We also proposed that the structure model of the film after the annealing at 510 K. The stoichiometry was Fe_8N_5 and the unit cell was denoted as $\begin{pmatrix} 3 & 5 \\ -5 & 8 \end{pmatrix}$.

Chapter 5

Electronic and magnetic properties of Fe_2N monolayer tuned by symmetry of substrates

5.1 Introduction

The magnetic properties of the ferromagnetic film such as coercivity, magnetic easy axis, and saturation magnetization have been tuned by the substrates [49, 108, 109]. The substrate changes the atomic distance between the film and the substrate as well as the inner atomic distance of the magnetic films. In addition, in a-few-monolayer level, the hybridization between the substrate and film [110, 111] and spin-orbit coupling [17, 112] also strongly affect the magnetic properties since a-few-monolayer films are strongly affected by the interaction with the substrates [17].

The superstructure also impacts on the electronic and magnetic properties of a-few-monolayer films. Some films with the robust bonding can grow incommensurately on the substrates and form the superstructures due to the difference in the lattice constant between the film and the substrate. They are observed in some systems such as FeO/Pt(111) [113], Ag/Cu(111) [114], Cu_2N/Cu(111) [69] and so on. The superstructure can induce the modulation of local density of states and magnetic properties of the film in addition to the structural modulation [114–116].

In Chapter 4, we have successfully fabricated the two new iron nitride films on the Cu(111) substrate. We found that one is the square Fe_2N monolayer on the Cu(111) substrate (Fe_2N/Cu(111)) similar to the square Fe_2N monolayer on the Cu(001) substrate (Fe_2N/Cu(001)). The lattice of Fe_2N/Cu(111) is

distorted toward a monoclinic lattice. In addition, the periodic lateral modulation is observed. It is expected that the magnetic moment of the square Fe_2N monolayer can be modified by the symmetry of the Cu substrate.

In this chapter, we report the local electronic properties of Fe_2N/Cu(111) studied by using STM/STS and magnetic properties obtained by using XAS/XMCD measurements. We found that the magnetic moment of Fe_2N/Cu(111) is smaller than that of Fe_2N/Cu(001). We compared the results of electronic and magnetic properties of Fe_2N/Cu(001) with those of Fe_2N/Cu(001) and discussed the origin of the magnetic properties tuned by the symmetry of the Cu substrates.

5.2 Experimental method

The detail of our STM measurement system is described in Chapter 3. The square Fe_2N/Cu(111) for the STM study was fabricated by the same way as that we established in Chapter 4. The Fe_2N/Cu(001) was fabricated by the following procedure as reported previously [15]. First, the clean Cu(001) substrate was obtained by repeating the cycle of Ar^+ sputtering and annealing at 900 K. Then, the Fe_2N/Cu(001) was fabricated by N^+ ion bombardment, 2 ML Fe deposition in UHV and subsequent annealing at 580 K.

The XAS/XMCD measurements were conducted at UVSOR-Ⅲ BL-4B [66, 67]. The measurement system is shown in Chapter 3. At this measurement, the degree of the circular polarization was 50%. For XAS/XMCD study, the Fe_2N monolayers were prepared in a similar way to that for the STM/STS measurements. The well-ordered Fe_2N monolayers were confirmed by the sharp spots of LEED pattern. Here, the coverage of Fe_2N/Cu(111) was 0.8 ± 0.2 ML, which was estimated from the LEED spot intensities of the Fe_2N monolayer compared with those of the Cu(111) substrate.

5.3 Results and Discussion

5.3.1 Electronic structure

First, we measured the spatially-averaged dI/dV spectra of Fe_2N/Cu(001) and Fe_2N/Cu(111). The dI/dV spectra are shown in Fig. 5.1 (a). Both in the dI/dV spectra of Fe_2N/Cu(001) and Fe_2N/Cu(111), broad shoulder structures appear below E_F. In contrast, the shoulder structure above E_F is only observed on Fe_2N/Cu(001). Here, E_F is located at 0 V.

Figure 5.1 (b) displays the tunneling current dependence on the dI/dV spectra of Fe_2N/Cu(111). The shoulder structure below E_F became a distinct

peak as increasing the tunneling current of the set point, *i.e.* decreasing the tip-surface distance. As described in Chapter 4, the tunneling probability to the inner d states becomes higher with decreasing the tip-sample distance. Therefore, the prominent peak at the short tip-sample distance indicates that the peak below E_F is mainly attributed to the $3d$ states of the Fe_2N monolayer.

The feature of the dI/dV spectra of Fe_2N/Cu(111) was changed along the stripe superstructure as shown in Fig. 5.1 (c). The peak just below E_F measured at the apparently-low regions is slightly broader than that at the apparently-high regions. In addition, the peak position obtained at the apparently-low regions shifts toward the higher binding energy. As seen in Chapter 4, the actual height is corrugated along the stripe superstructure. According to the calculation, the local density of states of $3d$ orbitals of the Fe_2N monolayer near E_F strongly affect the local hybridization with the substrates [14,15]. At the low regions where the actual distance between the Fe_2N monolayer and the Cu(111) substrate is low, the hybridization of Fe atoms with the Cu atoms is stronger than at the high regions. Therefore, the difference in the dI/dV curve between the low and high regions is attributed to the difference in the local hybridization.

In order to investigate the difference of the unoccupied states between Fe_2N/Cu(001) and Fe_2N/Cu(111), we have investigated the XA spectra of N K edge by irradiating linear polarized light without external magnetic field as shown in Fig. 5.2 (a). In the case of the XA spectra of N K edge of Fe_2N/Cu(001), two distinct peaks denoted as peaks A and B in Fig. 5.2 (a) are located at 397.2 eV and 400.3 eV both at $\theta = 0°$ and 55°. Here, θ is defined as the angle between the surface normal direction and the X-ray incidence direction. The XA spectrum of N K edge of Fe_2N/Cu(111) at $\theta = 0°$ also has two distinct peaks at almost the same energy as that of Fe_2N/Cu(001). In contrast, those at $\theta = 55°$ and 70° have an additional shoulder structure at 399.0 eV denoted as A′ in Fig. 5.2 (a). The shoulder structure becomes prominent with increasing θ. The intensity of peak B decreases with increasing θ both at Fe_2N/Cu(001) and Fe_2N/Cu(111).

As seen in Chapter 4, the N atoms are distributed at various sites of the Cu(111) substrate. We consider that the N atoms at the atop sites of the Cu(111) substrate have similar local electronic structure to those on the Cu(001) substrate since the closest Fe and Cu atoms from the N atoms are the same as those on the Cu(001) substrate. Therefore, the peak A which appeared both on the Cu(001) and Cu(111) substrates is attributed to the N atoms located at the atop sites of the Cu substrates. The shoulder structure at A′ is attributed to be the distribution of the local electronic structure of the N atoms since the N atoms are located at other sites such as hollow sites and bridge sites. Similar sites and incident-angle dependence of XAS is previously

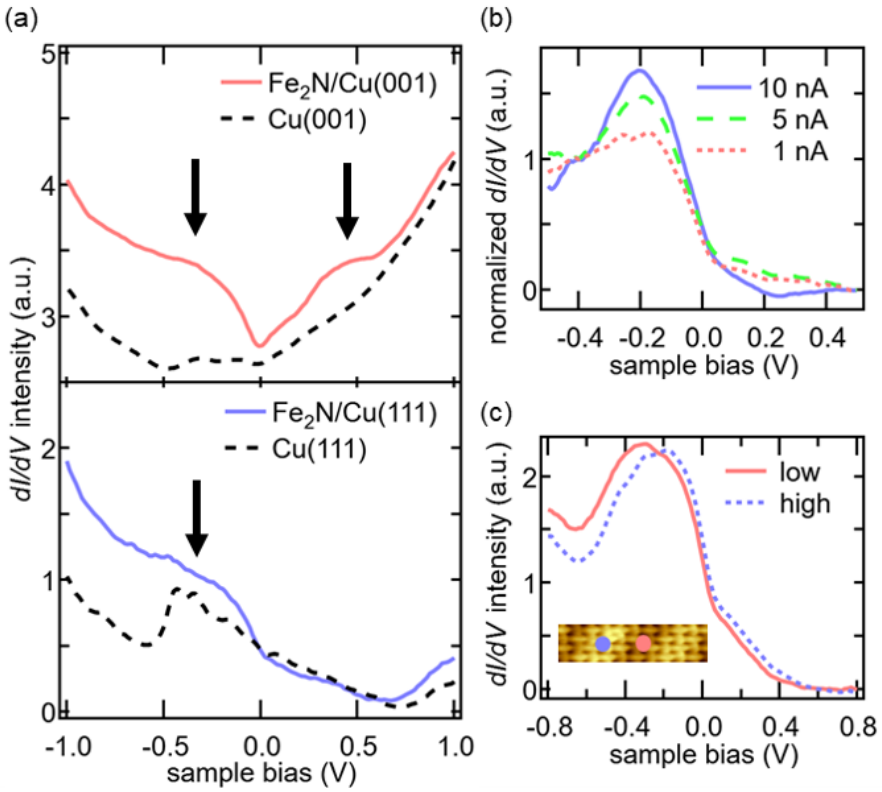

Figure 5.1: (a) The dI/dV spectra of Fe_2N/Cu(001) (a red line) and Fe_2N/Cu(111) (a blue line). Black dotted lines indicate the dI/dV spectra at each clean Cu regions. These dI/dV spectra of the Fe_2N monolayer and Cu substrate are obtained by using the same tip. The STM tip was stabilized at $V_B = 1.5$ V and $I_t = 2.0$ nA in the case of Fe_2N/ Cu(001) and at $V_B = 1.0$ V and $I_t = 2.0$ nA in the case of Fe_2N/Cu(111). The black arrows indicate the shoulder structures. (b) Tip-height dependence of the dI/dV spectra for Fe_2N/Cu(111). During the measurement, the tip was stabilized at $V_B = 200$ mV and $I_t = 1$, 5, and 10 nA. (c) The dI/dV spectra recorded at the two circles on the inset topographic STM image with the tip-stabilized condition of $V_B = 200$ mV and $I_t = 8.0$ nA.

reported for a graphene on the Ni(111) substrate [117].

The dI/dV spectra of Fe_2N/Cu(111) and Fe_2N/Cu(001) have a peak at +3.2 V and 3.3 V, respectively as shown in Fig. 5.2 (b). The peak B of the XA spectra is also located at about 3 eV higher than E_F. The density functional calculation for a γ'-Fe_4N which includes a square Fe_2N plane suggests that the N-Fe antibonding state of the γ'-Fe_4N is located at around +3.5 V [9]. The distinct peak of the dI/dV spectra is also observed at the Cu_2N monolayer [118, 119] and the hexagonal iron nitride monolayer on the Cu(001) substrate [16]. The origin of the peak B could be the Fe and N antibonding states.

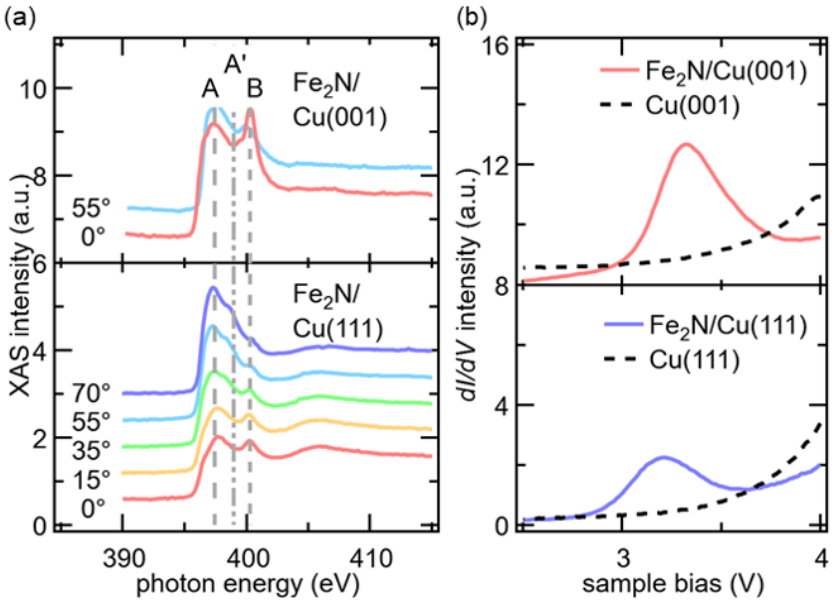

Figure 5.2: (a) N K edge XA spectra of (upper) Fe_2N/Cu(001) and (lower) Fe_2N/Cu(111). The linear background estimated from the pre-edge region was subtracted from each raw spectrum. (b) The dI/dV spectra of (upper) Fe_2N/Cu(001) and (lower) Fe_2N/Cu(111) recorded at $V_B = 4.0$ V and $I_t = 2.0$ nA. The spectra on the clean Cu regions are shown as dotted curves.

5.3.2 Magnetic properties

The XA spectra and XMCD of Fe $L_{2,3}$ edge of Fe_2N/Cu(111) are shown in Fig. 5.3 (a). They are obtained at 8 K by irradiating left-handed and right banded circularly polarized light under external magnetic field $B = \pm 5$ T. The surface is irradiated from the normal incidence $\theta = 0°$, or from the grazing incidence, $\theta = 55°$. Here, μ_+ (μ_-) is defined as the spectrum obtained by X-ray helicity parallel (antiparallel) to the direction of Fe3d majority spin. The strong XMCD signals indicate that Fe_2N/Cu(111) exhibits ferromagnetism. The intensity of the XMCD signal at the grazing incidence is similar to that at the normal incidence. The orbital magnetic moment and effective spin magnetic moment estimated by applying XMCD sum rule [23, 24] are shown in Table 5.1. Here, the average number of Fe3d holes is 3.2. Compared with the effective spin magnetic moment of Fe_2N/Cu(001) of 1.1 μ_B/atom [15], that of Fe_2N/Cu(001) became less than half.

The magnetization curve of Fe_2N/Cu(111) was obtained by plotting the ratio of L_3 peak intensity to L_2 one against the external magnetic field. The magnetization curves both at the grazing and normal incidence are saturated at more than 3 T. In contrast to the magnetization curve of Fe_2N/Cu(001) which shows the strong in plane magnetic anisotropy, the magnetization curve

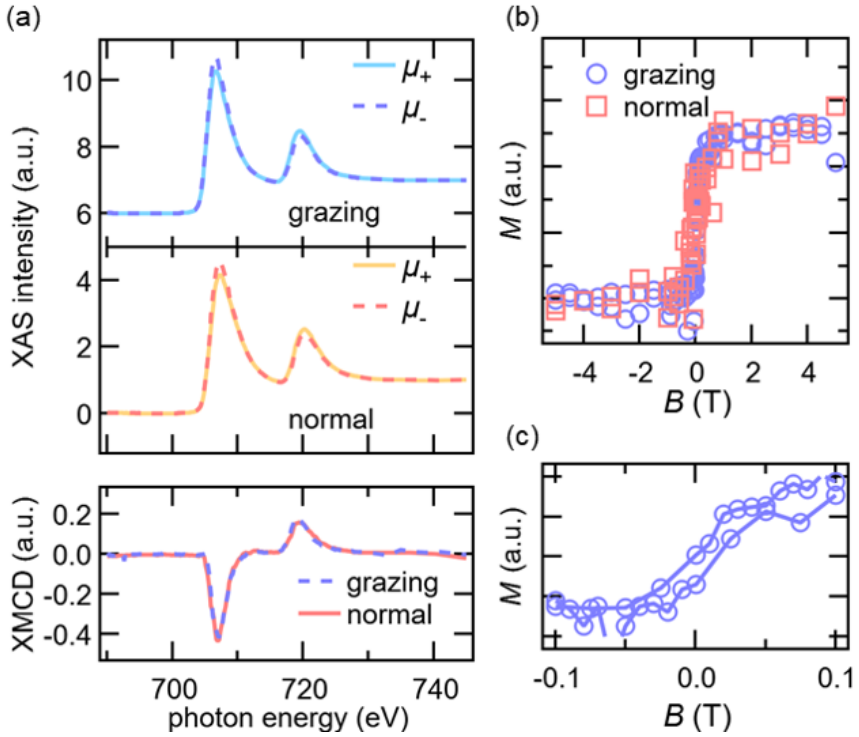

Figure 5.3: (a) (upper) XA spectra of Fe $L_{2,3}$ edge of Fe_2N/Cu(111) in the grazing incidence and normal incidence. (lower) XMCD spectra obtained from the XA spectra. (b) Magnetization curves of Fe_2N/Cu(111) in the grazing incidence indicated by blue circles and normal incidence indicated by red squares. (c) The magnetization curve in the range of -0.1 T to 0.1 T at the grazing incidence.

of Fe_2N/Cu(111) at the grazing incidence was similar to that at the normal incidence. It means that the magnetic anisotropy became weak at Fe_2N/Cu(111). The coercivity was approximately 20 mT in the grazing incidence as shown in Fig. 5.3 (c). Due to the symmetry difference between the square Fe_2N monolayer and the hexagonal Cu(111) substrate, we observed the six equivalent structural domains and the average structure domain size was at most 10×10 nm^2. In contrast, in the case of Fe_2N/Cu(001), the uniform structural domain is formed in larger than 100×100 nm^2. We consider that the small structural domain size causes the small magnetic domain and weakens the magnetic anisotropy.

Strong hybridization between the films of 3*d* metal and substrates generally reduces the exchange splitting of the 3*d* band and reduces the spin magnetic moment [120]. This is true for a-few-monolayer iron nitride. According to the theoretical calculation, the hybridization between the iron nitride film and the Cu(001) substrate actually reduces the spin magnetic moment [15].

Table 5.1: Effective spin magnetic moment $m_{\mathrm{spin}}^{\mathrm{eff}}$ and orbital magnetic moment m_{orb} of Fe_2N/Cu(111) and Fe_2N/Cu(001)

		$m_{\mathrm{spin}}^{\mathrm{eff}}$ (μ_B/atom)	m_{orb} (μ_B/atom)
Fe_2N/Cu(111)	0°	0.45(10)	0.06(5)
	55°	0.51(10)	0.05(5)
Fe_2N/Cu(001) [15]	0°	0.95	0.06
	55°	1.1	0.07

We observed the different feature of the spatially-averaged dI/dV spectra as shown in Fig. 5.1 (a). This indicates that the hybridization between the Fe_2N monolayer and the Cu(111) substrate is different from that between the Fe_2N monolayer and the Cu(001) substrate. Therefore, we consider that one of the reason for the reduction of the spin magnetic moment is the difference in the hybridization of the Fe_2N monolayer with the Cu substrates.

In addition, the spatial modulation of the local density of states are observed in the dI/dV spectra shown in Fig. 5.1 (c) and N K edge spectra shown in Fig. 5.2 (a) because of the spatial hybridization induced by the difference in the gap between the substrates and the film. We consider that other reason for the reduction of moment is the spatial modulation in the hybridization which is induced by the actual spatial modulation of the Fe_2N monolayer on the C(111) substrates. In fact, it is reported that the modulation of the local density of states of the ferromagnetic films induces the spatial modulation of the magnetic moment [115, 116].

In Chapter 4, we described that the Fe_2N monolayer on the Cu(111) substrate is distorted by the lattice mismatch between the film and the substrate. The distortion also changes the magnetic moment of the film near the interface. According to the experimental results, the lattice distortion of γ'-Fe_4N decreases the saturation magnetization by more than 10% [49]. Therefore, we consider that the lattice distortion affect the reduction of the magnetic moment as well as the spatial hybridization difference.

From the XPS measurement in Chapter4, the electric configuration of Fe in the Fe_2N monolayer is $3d^6 4s^2$. According to the first-principle calculations, the Fe3d orbitals of $c(2\times2)$ Fe_2N/Cu(001) split as shown in Fig. 5.4 (a). Here, x and y axis denote the in-plane direction and z axis denotes the out-of-plane direction as indicated in Fig. 5.4 (b). The density of state of d_{xy} orbital spreads broadly compared with other orbitals. From the crystal field theory, this indicates that the states of Fe are more strongly affected by the neighbor Fe and N atoms than by the neighbor Cu atoms. However, since it is difficult to predict the splitting width of Fe3d orbitals by the crystal field theory and

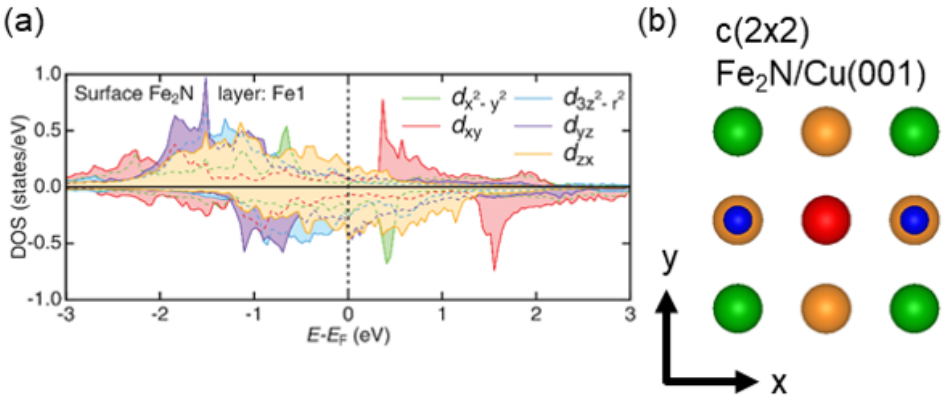

Figure 5.4: (a) The calculated electronic states of the $c(2\times2)Fe_2N$ monolayer on the Cu(001) substrate [15]. (b) Atomic structure around an Fe atom indicated by a red ball. Schematic model of $c(2\times2)Fe_2N$ are shown. Green, blue and orange balls show the Fe, N, and Cu atoms respectively. (a): taken from Fig. 7 (b) in [15]

Fe atoms of Fe_2N/Cu(111) are located at the low-symmetry sites, we could not describe the reduction of the magnetic moment of Fe_2N/Cu(111) by the crystal field theory. Further calculations would be necessary to get a better understanding.

5.4 Summary

We have investigated the difference in the local density of states and magnetic properties between Fe_2N/Cu(111) and Fe_2N/Cu(001). The dI/dV spectra of Fe_2N/Cu(111) indicates that the spatial modulation of the local density of $3d$ Fe states near E_F. This result was also supported by the shoulder structure of N K edge XA spectra of Fe_2N/Cu(111) which was not observed at Fe_2N/Cu(001). The effective spin magnetic moment of Fe of Fe_2N/Cu(111) became less than half of that of Fe_2N/Cu(001). The reasons for this are the difference in the hybridization and the lattice distortion induced by the substrates.

Appendix 5.A Curie temperature

We measured the XA spectra of Fe_2N/Cu(111) while the sample temperature was kept at around 40 K. Figure 5.5 shows the XA and XMCD spectra obtained at $B = 0$ T after the magnetic field $B = 5$ T was applied. In contrast to XMCD spectra at 8 K, XMCD spectra at 40 K does not have any peaks. This indicates

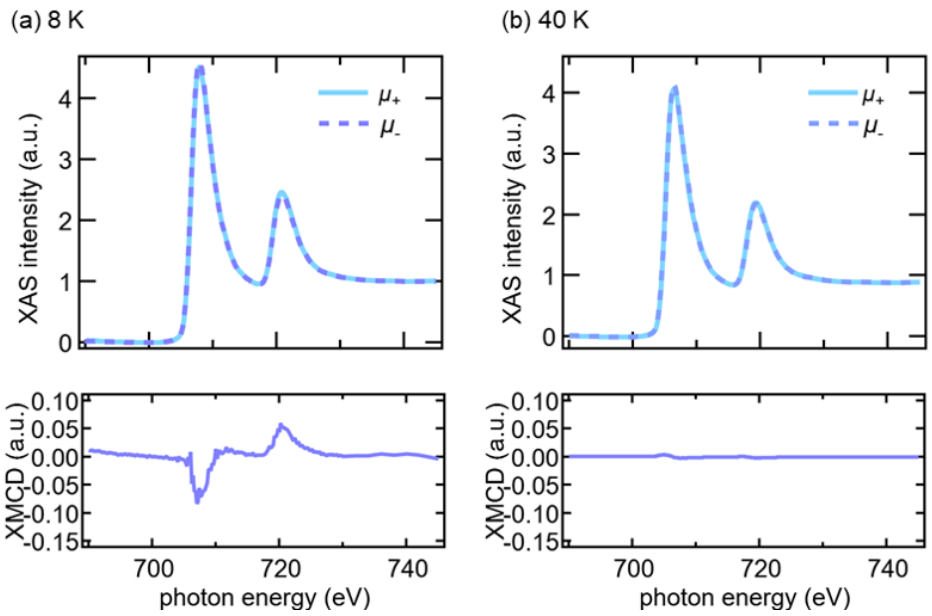

Figure 5.5: (a),(b) (upper) XA spectra of Fe_2N/Cu(111) at $B = 0$ T after magnetic field $B = 5$ T is applied. During the measurement, the sample temperature was kept at (a) 8 K and (b) 40 K. (lower) XMCD spectra obtained from the XA spectra.

that the Curie temperature of Fe_2N/Cu(111) is below 40 K. This value is lower than the Curie temperature of Fe_2N/Cu(001) which is about 80 K [121].

Appendix 5.B XAS/XMCD spectra of the dotted structure

As seen in Chapter 4, another iron nitride film which we call as dotted structure, is fabricated by the lower annealing temperature. We have also conducted XAS/XMCD measurements at UVSOR-Ⅲ BL-4B. The sample was fabricated by the same procedure as the STM measurements and the fabrication for the dotted structure was confirmed by the sharp spots of LEED pattern. However, as shown in Fig. 5.6, we did not observe the XMCD signal at 8 K which indicates the dotted structure exhibits paramagnetism.

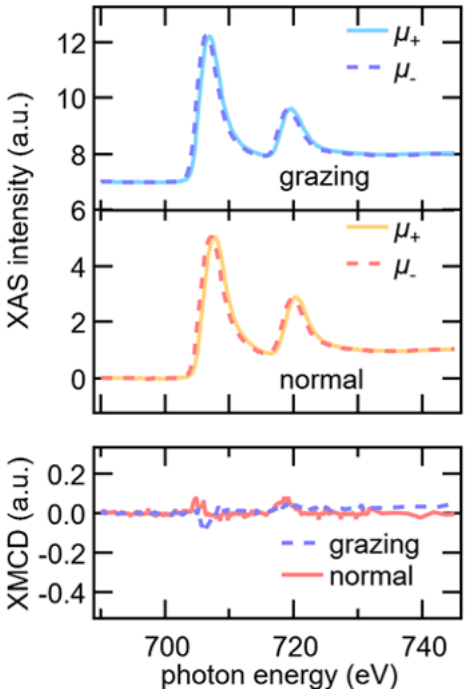

Figure 5.6: (upper) Fe $L_{2,3}$ edge XA spectra of the dotted structure at the grazing incidence and normal incidence. (lower) XMCD spectra obtained from the XA spectra.

Chapter 6

Enhancement of spin magnetic moment of iron nitride layers by mixing Co

The contents of this chapter will be published elsewhere within five years, and thus not open to the public in the abbreviated version.

Chapter 7

STM study of hexagonal iron nitride film on the Cu(111) substrate

The contents of this chapter will be published elsewhere within five years, and thus not open to the public in the abbreviated version.

Chapter 8

Summary and Conclusion

In summary, we have succeeded in fabricating a square iron nitride film and hexagonal one selectively on the Cu(111) substrate. We found that the magnetic properties of the square Fe_2N monolayer can be tuned by changing the symmetry of the substrates and making FeCo layer. The results in each chapter are summarized as follows.

1. Lattice distortion of square iron nitride monolayers induced by changing symmetry of Cu substrates

We fabricated two structures, the square Fe_2N monolayer and the Fe_8N_5 monolayer on the Cu(111) substrates depending on the annealing temperature. The former structure was similar to the square Fe_2N monolayer on the Cu(001) substrates. The difference in the symmetry between the square Fe_2N monolayer and hexagonal Cu(111) substrate distorted the Fe_2N monolayer toward a monoclinic lattice. We have proposed the structure model of these iron nitride monolayers.

2. Electronic and magnetic properties of Fe_2N monolayer tuned by symmetry of substrates

We have investigated the electronic and magnetic properties of the Fe_2N monolayer on the Cu(111) substrate by combining STM/STS with XAS/XMCD. The spin magnetic moment of the Fe_2N monolayer on the Cu(111) substrate was less than half of that on the Cu(001) substrates. The dI/dV spectra reveals that the density of states are modulated along the stripe superstructure.

3. Enhancement of spin magnetic moment of iron nitride layers by mixing Co

Not shown in the abbreviated version.

4. STM study of hexagonal iron nitride film on the Cu(111) substrate

Not shown in the abbreviated version.

The origin of the change in the magnetic moment has not completely been understood yet. We have elucidated two important factors. First is the distance between Fe and Cu atoms. We proposed that the local structural modulation changes the magnetic properties in Chapter 5. Second is the hybridization between the Fe atoms and the adjacent elements. As described in Chapter 6, we suggested that the hybridization between Fe and Cu decreases the magnetic moment of Fe. Our results will be greatly useful for revealing the origin of the magnetic properties by combining with further theoretical calculations.

Our new results would lead to the future experiment. It has been thought that the lattice constant of the film should be similar to that of the substrates. However, we demonstrate that the film with the robust in-plane bonding can grow independently on the symmetry of the substrates. It is expected that other monolayer films could also grow on various substrates. If it is achieved, the physical properties can be tuned through various substrates.

Acknowledgements

The present thesis has been carried out under the direction of Prof. Dr. Fumio Komori at the Institute for Solid State Physics, the University of Tokyo.

First of all, I wish to express my deepest gratitude to Prof. Dr. Fumio Komori for giving me constructive comments and warming encouragement all through the duration of present work. Then, I am deeply grateful to Dr. Toshio Miyamachi for giving me thoughtful advises and showing me attitude as a researcher.

I would like to offer my special thanks to the members of Komori group: Mr. Takushi Iimori, Mr. Norikazu Kawamura, Dr. Yoichi Otsuka, Dr. Masamichi Yamada, and Mr. Yuki Takahashi. I would like to thank the former members; Dr. Koichiro Ienaga, Dr. Yukio Takahashi, Dr. Shuhei Nakashima, Mr. Sougen Toyohisa, and Mr. Kaisyu Kawaguchi.

I also thank Prof. Dr. Toshihiko Yokoyama, Dr. Yasumasa Takagi, Dr. Takanori Koitaya, and Dr. Kohei Yamamoto for experimental supports during the beamtime in UVSORⅢ BL-4B.

I also appreciate Prof. Dr. Claus Michael Schneider, Dr. Daniel Bürgler, and Dr. Frank Matthes accepting me as a research student in Peter Grünberg Institute, Forschungszentrum Jülich for a three month.

I am grateful to Ms. Natsumi Ishibashi, Ms. Michiko Komaki, and Ms. Ikumi Saito for dealing with a lot of office works.

I would like to thank the financial supports by a Grant-in-Aid for Japan Society for the promotion of Science (JPSJ) Fellows (19J13518) from Ministry of Education, Culture, Sports, Science and Technology of Japan.

Finally, I would like to thank my parents and relatives for supporting my student life as well as research activities.

February 2020
Takuma Hattori

References

[1] J. D. Livingston, JOM **42**, 30 (1990).

[2] G. Scheunert, O. Heinonen, R. Hardeman, A. Lapicki, M. Gubbins, and R. M. Bowman, Appl. Phys. Rev. **3**, 011301 (2016).

[3] K. Honda and S. Saitô, Phys. Rev. **16**, 495 (1920).

[4] D. Givord, H. Li, and J. Moreau, Solid State Commun **50**, 497 (1984).

[5] C. Kim, W. Yoo, H.-W. Bang, S. Lee, Y. C. Park, Y. H. Lee, J. Choi, Y. Jo, K. Lee, and M.-H. Jung, ACS Omega **4**, 16578 (2019).

[6] S. Mizukami, A. Sakuma, A. Sugihara, K. Suzuki, and R. Ranjbar, Scr. Mater. **118**, 70 (2016).

[7] A. Sakuma, J. Magn. Magn. Mater. **102**, 127 (1991).

[8] J. Coey and P. Smith, J. Magn. Magn. Mater. **200**, 405 (1999).

[9] M. Sifkovits, H. Smolinski, S. Hellwig, and W. Weber, J. Magn. Magn. Mater. **204**, 191 (1999).

[10] J. M. Gallego, S. Y. Grachev, D. M. Borsa, D. O. Boerma, D. Écija, and R. Miranda, Phys. Rev. B **70**, 115417 (2004).

[11] T. K. Kim and M. Takahashi, Appl. Phys. Lett. **20**, 492 (1972).

[12] J. Coey, H. Sun, and D. Hurley, J. Magn. Magn. Mater. **101**, 310 (1991).

[13] T. Kumura, K. Yamauchi, and T. Kobayashi, J. Appl. Phys. **61**, 3844 (1987).

[14] Y. Takahashi, T. Miyamachi, K. Ienaga, N. Kawamura, A. Ernst, and F. Komori, Phys. Rev. Lett. **116**, 056802 (2016).

[15] Y. Takahashi, T. Miyamachi, S. Nakashima, N. Kawamura, Y. Takagi, M. Uozumi, V. N. Antonov, T. Yokoyama, A. Ernst, and F. Komori, Phys. Rev. B **95**, 224417 (2017).

[16] K. Ienaga, T. Miyamachi, Y. Takahashi, N. Kawamura, and F. Komori, Phys. Rev. B **96**, 085439 (2017).

[17] C. Gong and X. Zhang, Science **363**, (2019).

[18] G. Binnig, H. Rohrer, C. Gerber, and E. Weibel, Phys. Rev. Lett. **49**, 57 (1982).

[19] J. Tersoff and D. R. Hamann, Phys. Rev. B **31**, 805 (1985).

[20] J. Bardeen, Phys. Rev. Lett. **6**, 57 (1961).

[21] N. D. Lang, Phys. Rev. B **34**, 5947 (1986).

[22] D. A. Shirley, Phys. Rev. B **5**, 4709 (1972).

[23] B. T. Thole, P. Carra, F. Sette, and G. van der Laan, Phys. Rev. Lett. **68**, 1943 (1992).

[24] P. Carra, B. T. Thole, M. Altarelli, and X. Wang, Phys. Rev. Lett. **70**, 694 (1993).

[25] K. Momma and F. Izumi, J. Appl. Crystallogr. **44**, 1272 (2011).

[26] A. Leineweber, H. Jacobs, F. Hüning, H. Lueken, H. Schilder, and W. Kockelmann, J. Alloys Compd. **288**, 79 (1999).

[27] P. Schaaf, Prog. Mater Sci. **47**, 1 (2002).

[28] F. Haber and R. L. Rossignol, J. Ind. Eng. Chem. **5**, 328 (1913).

[29] P. H. Emmett, S. B. Hendricks, and S. Brunauer, J. Am. Chem. Soc. **52**, 1456 (1930).

[30] A. A. Noyes and L. B. Smith, J. Am. Chem. Soc. **43**, 475 (1921).

[31] K. H. Jack and C. F. Goodeve, Proc. R. Soc. London, Ser. A **195**, 34 (1948).

[32] K. H. Jack and C. F. Goodeve, Proc. R. Soc. London, Ser. A **208**, 216 (1951).

[33] K. H. Jack, Acta Crystallogr. **5**, 404 (1952).

[34] K. H. Jack, J. Appl. Phys. **76**, 6620 (1994).

[35] Y. Sugita, K. Mitsuoka, M. Komuro, H. Hoshiya, Y. Kozono, and M. Hanazono, J. Appl. Phys. **70**, 5977 (1991).

[36] B. C. Frazer, Phys. Rev. **112**, 751 (1958).

[37] H. Jacobs, D. Rechenbach, and U. Zachwieja, J. Alloys Compd. **227**, 10 (1995).

[38] G. Shirane, W. J. Takei, and S. L. Ruby, Phys. Rev. **126**, 49 (1962).

[39] C. Kuhnen, R. de Figueiredo, V. Drago, and E. da Silva, J. Magn. Magn. Mater. **111**, 95 (1992).

[40] S. Nagakura, J. Phys. Soc. Jpn. **25**, 488 (1968).

[41] S. Matar, B. Siberchicot, M. Pénicaud, and G. Demazeau, J. Phys. I France **2**, 1819 (1992).

[42] T. Hinomura and S. Nasu, Hyperfine Interact. **111**, 221 (1998).

[43] D. Rechenbach and H. Jacobs, J. Alloys Compd. **235**, 15 (1996).

[44] E. Lehrer, Z Elektrochem. Anger. Phys. Chem. **36**, 460 (1930).

[45] J. L. Costa-Krämer, D. M. Borsa, J. M. García-Martín, M. S. Martín-González, D. O. Boerma, and F. Briones, Phys. Rev. B **69**, 144402 (2004).

[46] K. Ito, G. H. Lee, K. Harada, M. Suzuno, T. Suemasu, Y. Takeda, Y. Saitoh, M. Ye, A. Kimura, and H. Akinaga, Appl. Phys. Lett. **98**, 102507 (2011).

[47] L. Wang, X. Wang, N. Ma, W. Zheng, D. Jin, and Y. Zhao, Surf. Coat. Technol. **201**, 786 (2006).

[48] T. Yamaguchi, M. Sakita, M. Nakamura, and T. Kobira, J. Magn. Magn. Mater. **215-216**, 529 (2000).

[49] S. Atiq, H.-S. Ko, S. A. Siddiqi, and S.-C. Shin, Appl. Phys. Lett. **92**, 222507 (2008).

[50] K. Yamaguchi, T. Yui, K. Yamaki, I. Kakeya, K. Kadowaki, and T. Suemasu, J. Cryst. Growth **301-302**, 597 (2007).

[51] H. Fang, R. Zhang, B. Liu, Z. Tao, X. Wang, Z. Xie, X. Xiu, and Y. Zheng, J. Phys. D: Appl. Phys. **45**, 315002 (2012).

[52] Y. Qi, X. Liu, W. Huang, H. Lu, and J. Gao, Vacuum **133**, 13 (2016).

[53] S. Kokado, N. Fujima, K. Harigaya, H. Shimizu, and A. Sakuma, Phys. Rev. B **73**, 172410 (2006).

[54] A. Narahara, K. Yamaguchi, and T. Suemasu, J. Cryst. Growth **309**, 25 (2007).

[55] D. M. Borsa, S. Grachev, C. Presura, and D. O. Boerma, Appl. Phys. Lett. **80**, 1823 (2002).

[56] H. Nakagawa, S. Nasu, H. Fujii, M. Takahashi, and F. Kanamaru, Hyperfine Interact. **69**, 455 (1992).

[57] K. Suzuki, H. Morita, T. Kaneko, H. Yoshida, and H. Fujimori, J. Alloys Compd. **201**, 11 (1993).

[58] E. B. Easton, T. Buhrmester, and J. Dahn, Thin Solid Films **493**, 60 (2005).

[59] T. Hinomura and S. Nasu, Physica B **237-238**, 557 (1997).

[60] W. Lin, J. Pak, D. C. Ingram, and A. R. Smith, J. Alloys Compd. **463**, 257 (2008).

[61] C. Navio, J. Alvarez, M. J. Capitan, F. Yndurain, and R. Miranda, Phys. Rev. B **78**, 155417 (2008).

[62] Y. Takagi, K. Isami, I. Yamamoto, T. Nakagawa, and T. Yokoyama, Phys. Rev. B **81**, 035422 (2010).

[63] I. Ekvall, E. Wahlström, D. Claesson, H. Olin, and E. Olsson, Meas. Sci. Technol. **10**, 11 (1999).

[64] I. Horcas, R. Fernández, J. M. Gómez-Rodríguez, J. Colchero, J. Gómez-Herrero, and A. M. Baro, Rev. Sci. Instrum. **78**, 013705 (2007).

[65] D. Nečas and P. Klapetek, Cent. Eur. J. Phys. **10**, 181 (2012).

[66] T. Gejo, Y. Takata, T. Hatsui, M. Nagasono, H. Oji, N. Kosugi, and E. Shigemasa, Chem. Phys. **289**, 15 (2003).

[67] T. Nakagawa, Y. Takagi, Y. Matsumoto, and T. Yokoyama, Jpn, J. Appl. Phys. **47**, 2132 (2008).

[68] F. Leibsle, S. Dhesi, S. Barrett, and A. Robinson, Surf. Sci. **317**, 309 (1994).

[69] H. Baek, S. Sangjun, K. Jungpil, and J. Young, Seo, J. Korean Phys. Soc. **56**, 620 (2010).

[70] A. Brodde, K. Dreps, J. Binder, C. Lunau, and H. Neddermeyer, Phys. Rev. B **47**, 6609 (1993).

[71] M. Sotto, S. Gauthier, F. Pourmir, S. Rousset, and J. Klein, Surf. Sci. **371**, 36 (1997).

[72] R. Peng, H. C. Xu, S. Y. Tan, H. Y. Cao, M. Xia, X. P. Shen, Z. C. Huang, C. H. P. Wen, Q. Song, T. Zhang, B. P. Xie, X. G. Gong, and D. L. Feng, Nat. Commun. **5**, 5044 (2014).

[73] W. Zhou, Y. Liu, Y. Yang, and P. Wu, J. Phys. Chem. C **118**, 6448 (2014).

[74] A. Walsh, C. R. A. Catlow, K. H. L. Zhang, and R. G. Egdell, Phys. Rev. B **83**, 161202 (2011).

[75] R. F. C. Farrow, D. Weller, R. F. Marks, M. F. Toney, A. Cebollada, and G. R. Harp, J. Appl. Phys. **79**, 5967 (1996).

[76] L. Ranno, A. Llobet, R. Tiron, and E. Favre-Nicolin, Appl. Surf. Sci. **188**, 170 (2002).

[77] J. Lee, G. Lauhoff, M. Tselepi, S. Hope, P. Rosenbusch, J. A. C. Bland, H. A. Dürr, G. van der Laan, J. P. Schilléand, and J. A. D. Matthew, Phys. Rev. B **55**, 15103 (1997).

[78] T. Kozawa, T. Kachi, H. Kano, H. Nagase, N. Koide, and K. Manabe, J. Appl. Phys. **77**, 4389 (1995).

[79] H. Zhang, ACS Nano **9**, 9451 (2015).

[80] A. K. Geim and I. V. Grigorieva, Nature **499**, 419 (2013).

[81] C. Gong, L. Li, Z. Li, H. Ji, A. Stern, Y. Xia, T. Cao, W. Bao, C. Wang, Y. Wang, Z. Q. Qiu, R. J. Cava, S. G. Louie, J. Xia, and X. Zhang, Nature **546**, 265 (2017).

[82] B. Huang, G. Clark, E. Navarro-Moratalla, D. R. Klein, R. Cheng, K. L. Seyler, D. Zhong, E. Schmidgall, M. A. McGuire, D. H. Cobden, W. Yao, D. Xiao, P. Jarillo-Herrero, and X. Xu, Nature **546**, 270 (2017).

[83] Z. Fei, B. Huang, P. Malinowski, W. Wang, T. Song, J. Sanchez, W. Yao, D. Xiao, X. Zhu, A. F. May, W. Wu, D. H. Cobden, J.-H. Chu, and X. Xu, Nat. Mater. **17**, 778 (2018).

[84] M. Ormaza, L. Fernández, M. Ilyn, A. Magaña, B. Xu, M. J. Verstraete, M. Gastaldo, M. A. Valbuena, P. Gargiani, A. Mugarza, A. Ayuela, L. Vitali, M. Blanco-Rey, F. Schiller, and J. E. Ortega, Nano Lett. **16**, 4230 (2016).

[85] A. Cavallin, L. Fernández, M. Ilyn, A. Magaña, M. Ormaza, M. Matena, L. Vitali, J. E. Ortega, C. Grazioli, P. Ohresser, S. Rusponi, H. Brune, and F. Schiller, Phys. Rev. B **90**, 235419 (2014).

[86] V. Higgs, P. Hollins, M. Pemble, and J. Pritchard, J. Electron. Spectrosc. Relat. Phenom. **39**, 137 (1986).

[87] R. P. J.J. Mccarroll, T. Edmonds, Nature **223**, 1260 (1969).

[88] C. Klink, I. Stensgaard, F. Besenbacher, and E. Lægsgaard, Surf. Sci. **342**, 250 (1995).

[89] M. Foss, R. Feidenhans'l, M. Nielsen, E. Findeisen, R. L. Johnson, T. Buslaps, I. Stensgaard, and F. Besenbacher, Phys. Rev. B **50**, 8950 (1994).

[90] J. C. Fuggle and N. Martensson, J. Electron. Spectrosc. Relat. Phenom. **21**, 275 (1980).

[91] Y. Hashimoto, K. Nakatsuji, T. Iimori, and F. Komori, Surf. Sci. **604**, 451 (2010).

[92] X. Wang, W. Zheng, H. Tian, S. Yu, W. Xu, S. Meng, X. He, J. Han, C. Sun, and B. Tay, Appl. Surf. Sci. **220**, 30 (2003).

[93] W. Zhong, B. Tay, S. Lau, X. Sun, S. Li, and C. Sun, Thin Solid Films **478**, 61 (2005).

[94] K. Kim, J. Electron Spectrosc. Relat. Phenom. **3**, 217 (1974).

[95] G. van der Laan, C. Westra, C. Haas, and G. A. Sawatzky, Phys. Rev. B **23**, 4369 (1981).

[96] A. P. Grosvenor, B. A. Kobe, M. C. Biesinger, and N. S. McIntyre, Surf. Interface Anal. **36**, 1564 (2004).

[97] P. C. Graat and M. A. Somers, Appl. Surf. Sci. **100-101**, 36 (1996).

[98] E. J. Miola, S. D. de Souza, P. A. Nascente, M. Olzon-Dionysio, C. A. Olivieri, and D. Spinelli, Appl. Surf. Sci. **144-145**, 272 (1999).

[99] B. D and M. Seah, *Practical Surface Analysis. Volume 1. Auger and X-ray Photoelectron Spectroscopy* (Wiley, 1996), Vol. 1.

[100] J. M. Gallego, D. O. Boerma, R. Miranda, and F. Ynduráin, Phys. Rev. Lett. **95**, 136102 (2005).

[101] R. L. Park and H. H. Madden, Surf. Sci. **11**, 188 (1968).

[102] D. Spišák and J. Hafner, Phys. Rev. B **67**, 235403 (2003).

[103] A. Soon, L. Wong, M. Lee, M. Todorova, B. Delley, and C. Stampfl, Surf. Sci. **601**, 4775 (2007).

[104] D. Friebel, C. Schlaup, P. Broekmann, and K. Wandelt, Phys. Chem. Chem. Phys. **9**, 2142 (2007).

[105] C. Hagendorf, R. Shantyr, H. Neddermeyer, and W. Widdra, Phys. Chem. Chem. Phys. **8**, 1575 (2006).

[106] J. Klikovits, E. Napetschnig, M. Schmid, N. Seriani, O. Dubay, G. Kresse, and P. Varga, Phys. Rev. B **76**, 045405 (2007).

[107] M. Bradley, D. Woodruff, J. Robinson, D. Sheppard, and A. Hentz, Surf. Sci. **635**, 27 (2015).

[108] A. M. Zhang, Z. X. Chen, W. Q. Zou, B. Lv, J. J. Ge, H. L. Cai, J. Du, X. S. Wu, S. J. Zhang, and S. M. Zhou, J. Appl. Phys. **111**, 07A704 (2012).

[109] Q. Gan, R. A. Rao, C. B. Eom, L. Wu, and F. Tsui, J. Appl. Phys. **85**, 5297 (1999).

[110] B. Újfalussy, L. Szunyogh, and P. Weinberger, Phys. Rev. B **54**, 9883 (1996).

[111] H. Dürr, G. van der Laan, D. Spanke, F. Hillebrecht, N. Brookes, and J. Goedkoop, Surf. Sci. **377-379**, 466 (1997).

[112] C. U. Jung, H. Yamada, M. Kawasaki, and Y. Tokura, Appl. Phys. Lett. **84**, 2590 (2004).

[113] M. Ritter, W. Ranke, and W. Weiss, Phys. Rev. B **57**, 7240 (1998).

[114] J. Bork, P. Wahl, L. Diekhöner, and K. Kern, New J. Phys. **11**, 113051 (2009).

[115] F. Meier, K. von Bergmann, P. Ferriani, J. Wiebe, M. Bode, K. Hashimoto, S. Heinze, and R. Wiesendanger, Phys. Rev. B **74**, 195411 (2006).

[116] R. Decker, J. Brede, N. Atodiresei, V. Caciuc, S. Blügel, and R. Wiesendanger, Phys. Rev. B **87**, 041403 (2013).

[117] M. Weser, Y. Rehder, K. Horn, M. Sicot, M. Fonin, A. B. Preobrajenski, E. N. Voloshina, E. Goering, and Y. S. Dedkov, Appl. Phys. Lett. **96**, 012504 (2010).

[118] L. Triguero and L. G. Pettersson, Surf. Sci. **398**, 70 (1998).

[119] C. D. Ruggiero, T. Choi, and J. A. Gupta, Appl. Phys. Lett. **91**, 253106 (2007).

[120] O. Hjortstam, J. Trygg, J. M. Wills, B. Johansson, and O. Eriksson, Phys. Rev. B **53**, 9204 (1996).

[121] Y. Takahashi, T. Miyamachi, T. Yokoyama, and F. Komori (unpublished).